Research Square

Preprints are preliminary reports that have not undergone peer review.
They should not be considered conclusive, used to inform clinical practice,
or referenced by the media as validated information.

An off-the-shelf light-sheet microscopy ecosystem enables versatile cleared-tissue imaging across scales and applications

Etsuo Susaki

suishess-kyu@umin.ac.jp

Juntendo University https://orcid.org/0000-0001-5621-7311

Yuki Nozawa

Juntendo University

Steven Edwards

KTH Royal Institute of Technology https://orcid.org/0000-0001-7930-7977

Kiyotada Naitou

Kagoshima University https://orcid.org/0000-0001-8599-2528

Maximilian Senftleben

KTH Royal Institute of Technology

Akira Yoshikawa

Juntendo University https://orcid.org/0009-0000-1510-6447

Yukihiko Sato

Juntendo University

Yuri Saito

Juntendo University

Yuichi Wada

Juntendo University https://orcid.org/0009-0004-5158-1244

Takenobu Nii

Kyushu University

Chikara Meno

Kyushu University https://orcid.org/0000-0002-0869-6642

Kohei Otomo

Juntendo University https://orcid.org/0000-0002-5322-6295

Hjalmar Brismar

KTH - Royal Institute of Technology https://orcid.org/0000-0003-0578-4003

Article

Keywords:

Posted Date: August 21st, 2026

DOI: https://doi.org/10.21203/rs.3.rs-10448090/v1

License: This work is licensed under a Creative Commons Attribution 4.0 International License.
Read Full License

Additional Declarations: Yes there is potential Competing Interest. E.A.S. receives long-term large-scale research funding from the Nakatani Foundation for FY2024–2028. E.A.S. is an executive officer and employee of CUBICStars Inc., a company that provides services based on CUBIC technology. E.A.S. is also named as a co-inventor on patents and patent applications owned by RIKEN and CUBICStars Inc., related to CUBIC reagents. The other authors declare no competing interests.

An off-the-shelf light-sheet microscopy ecosystem enables versatile cleared-tissue imaging across scales and applications

Authors:

Yuki Nozawa[1, 3]†, Steven Edwards[7]†, Kiyotada Naitou†[9]*, Maximilian Senftleben[7]†, Akira L. Yoshikawa[2, 3, 10, 11], Yukihiko Sato[2, 3], Yuri Saito[2, 3], Yuichi Wada[1, 2, 3], Takenobu Nii[12], Chikara Meno[12], Kohei Otomo[1, 2, 3, 4, 5], Hjalmar Brismar[7, 8]*, and Etsuo A. Susaki[1, 2, 3, 6]*

Affiliations:

1. Department of Biochemistry II, Faculty of Medicine, Juntendo University, 2-1-1 Hongo, Bunkyo-ku, Tokyo 113-8421, Japan.
2. Department of Biochemistry and Systems Biomedicine, Graduate School of Medicine, Juntendo University, 2-1-1 Hongo, Bunkyo-ku, Tokyo 113-8421, Japan.
3. Nakatani Biomedical Spatialomics Hub, Graduate School of Medicine, Juntendo University, 2-1-1 Hongo, Bunkyo-ku, Tokyo 113-8421, Japan.
4. Biophotonics Research Division, National Institute for Physiological Sciences (NIPS), National Institutes of Natural Sciences, 38 Nishigonaka, Myodaiji, Okazaki, Aichi 444-8585, Japan.
5. Biophotonics Research Group, Exploratory Research Center on Life and Living Systems (ExCELLS), National Institutes of Natural Sciences, 5-1 Higashiyama, Myodaiji, Okazaki, Aichi 444-8787, Japan.
6. Institute for Quantum Life Science, National Institutes for Quantum Science and Technology (QST), 4-9-1 Anagawa, Inage-ku, Chiba 263-8555, Japan.
7. Science for Life Laboratory, KTH Royal Institute of Technology, SE-171 65 Solna, Sweden.

8. Science for Life Laboratory, Karolinska Institute, SE-171 77 Stockholm, Sweden.
9. Department of Basic Veterinary Science, Joint Faculty of Veterinary Medicine, Kagoshima University, 1-21-24 Korimoto, Kagoshima 890-0065, Japan.
10. Department of Pathology, Kameda Medical Center, 929 Higashi-cho, Kamogawa City, Chiba 296-8602, Japan.
11. Department of Pathology Informatics, Nagasaki University Graduate School of Biomedical Sciences, 1-7-1 Sakamoto, Nagasaki 852-8501, Japan.
12. Department of Developmental Biology, Graduate School of Medical Sciences, Kyushu University, 3-1-1 Maidashi, Higashi-ku, Fukuoka 812-8582, Japan.

†Co-first authors

*Corresponding to

Kiyotada Naitou（k6845196@kadai.jp）

Hjalmar Brismar（hjalmar.brismar@scilifelab.se）

Etsuo A. Susaki (suishess-kyu@umin.ac.jp)

Abstract

Tissue clearing–based three-dimensional (3D) imaging has opened up organ- and body-wide 3D spatial biology, yet its broader adoption remains limited by the cost, complexity, and modality-specific fragmentation of high-end light-sheet fluorescence microscopy (LSFM). Existing systems force trade-offs among multicolor capability, resolution, field of view, and cost, splintering advanced imaging into separate, specialized instruments. Here we present an off-the-shelf LSFM ecosystem, descSPIM-Advanced, that unifies these capabilities as individually optimized yet interoperable variants within one accessible framework. Galaxy resolves 11 colors in phantoms and 7 in 3D samples without multi-round staining; Deepsky reaches ~1.09 μm lateral resolution for 3D histology of lung and kidney; Fullmoon provides a 23.8 mm × 28.1 mm field of view, capturing a tenfold-expanded whole mouse brain in a single field; and SLIM enables low-cost deployment (~US$15,000; assembled in 2–5 h). A shared Mission Control Center standardizes acquisition across configurations, democratizing versatile cleared-tissue imaging across scales and applications.

Introduction

Three-dimensional (3D) imaging of intact, cleared organs has become a fundamental technique in whole-organ and whole-body spatial biology, with applications across neuroscience, cancer biology, developmental biology, and drug discovery[1,2,3,4,5]. Early orthogonal-plane fluorescence optical sectioning established the conceptual basis of light-sheet imaging[6], and subsequent whole-brain imaging at cellular resolution demonstrated that large intact tissues could be visualized volumetrically without physical sectioning[7]. Together with rapid advances in related technologies, these developments shifted biological observation from selected sections toward comprehensive organ- and body-scale measurement[2,8]. Light-sheet fluorescence microscopy (LSFM) is particularly well suited to cleared-tissue imaging, providing optical sectioning, reduced photobleaching, and rapid volumetric acquisition over large specimens. Foundational selective-plane illumination microscopy (SPIM) and digitally scanned light-sheet microscopy (DSLM) established two major routes for generating thin excitation planes[9,10], and subsequent developments, including multidirectional illumination to reduce shadowing and striping artifacts[11], lateral tiling for field expansion[12,13], and axially swept illumination synchronized with rolling-shutter detection[14,15,16], have further improved image quality and usable imaging range.

Realizing this potential more broadly depends on making light-sheet microscopy accessible beyond specialized imaging facilities operating high-end commercialized systems. In this regard, open and low-cost LSFM platforms have broadened the practical adoption of light-sheet imaging: OpenSPIM, OpenSpinMicroscopy, the mesoSPIM initiative, and the more recent benchtop mesoSPIM implementation showed that light-sheet systems can be modular, reproducible, and disseminated through open, community-driven development [17,18,19,20], while other low-cost implementations, including miniSPIM, UC2, and projected light-sheet

microscopy, further emphasized affordability and ease of construction[21,22,23]. Building on this movement, we previously introduced descSPIM-basic, an affordable, easy-to-build, and expandable LSFM platform optimized for tissue-clearing applications[24]; by lowering barriers in cost, build complexity, and required optical expertise, descSPIM-basic helped move cleared-tissue LSFM from specialized facilities toward individual life-science laboratories, and has since been built in more than 40 laboratories worldwide. More recently, this accessibility-driven trajectory has begun to extend toward higher performance using inexpensive, off-the-shelf optics, including HySIL/SCOPE and a compact, aberration-corrected light-sheet microscope[25,26].

However, improving the performance of any single system does not address the varied and evolving demands of modern spatial biology. As descSPIM-basic was adopted across diverse experimental settings in individual laboratories, users increasingly requested capabilities beyond those of the original entry-level configuration. These requests converged on four recurring needs: an increased number of fluorescence channels (i.e., the number of simultaneously detectable molecular targets) resolvable within a single cleared specimen; higher spatial resolution for subcellular analysis in volumetric imaging; single-field imaging of larger cleared and expanded specimens to avoid extensive tiling, registration, and stitching; and simpler, faster, and lower-cost deployment from the basic design. Even the recent accessible systems noted above each provide only a single specialized capability through a dedicated instrument. Therefore, a unified accessible platform that brings these capabilities together has remained out of reach for most laboratories.

We reasoned that these capabilities need not be fragmented across separate machines, but could instead coexist as interoperable variants of a unified off-the-shelf platform under shared control software. Here we present descSPIM-Advanced, an expandable set of purpose-

optimized LSFM configurations built on the modular, customizable design of descSPIM-basic. Four representative implementations address the needs identified above: descSPIM-Galaxy targets fluorescence multiplexing, resolving 11 colors in optical phantoms and 7 colors in 3D biological samples without iterative multi-round staining; descSPIM-Deepsky provides higher spatial resolution through a configuration optimized for 3D histology of cleared tissues, reaching ~1.09 μm lateral resolution in lung and kidney; descSPIM-Fullmoon extends imaging coverage by enabling single-field volumetric imaging over a 23.8 mm × 28.1 mm field of view (FOV) of large cleared or tenfold-expanded specimens; and descSPIM-SLIM reduces deployment cost and complexity, offering a rapid-deployment configuration for routine multicolor cleared-tissue imaging (approximately US$15,000; assembled in 2–5 h). A shared Mission Control Center (MCC) provides unified control across these configurations, and complete construction guides, parts lists, analysis pipelines, and control software are released as open-source resources. We demonstrate the ecosystem across diverse cleared specimens and applications. Together, these implementations establish descSPIM-Advanced as a scalable platform for accessible cleared-tissue LSFM, bridging entry-level instrumentation and advanced, organ-scale 3D imaging within a single ecosystem.

Results

Design concept of the descSPIM-Advanced ecosystem

Built on the modular, off-the-shelf core of descSPIM-basic, descSPIM-Advanced comprises four purpose-optimized configurations; Galaxy, Deepsky, Fullmoon, and SLIM. Each address one of the four needs identified above (multiplexing, resolution, field of view, and low-cost deployment) by replacing or adding only the modules required for that capability, so that one laboratory can build, reconfigure, or upgrade between them. A shared Mission Control Center (MCC) operates descSPIM-basic and all four variants within a single open-source software

environment; we describe each configuration in turn below before integrating them into one accessible ecosystem.

descSPIM-Galaxy: A multi-excitation, multi-spectral configuration for multiplex cleared tissue imaging

To address the need for further multiplex cleared tissue imaging without iterative multi-round staining, we developed descSPIM-Galaxy, extending the capability of descSPIM-basic by increasing the number of fluorophores detectable. We designed the system around two complementary strategies: expanding the excitation wavelength range from the near-ultraviolet to the near-infrared region and separating overlapped emission spectra by hyperspectral imaging and linear unmixing[27]. For this purpose, 405 and 730 nm laser light sources and a hyperspectral camera were added to the configuration of descSPIM-basic, which utilized 488, 561, and 647 nm laser light sources and a CMOS camera. Five excitation wavelengths (405, 488, 561, 647 and 730 nm) were combined into a single illumination arm (**Supplementary Fig. 1**). The merged beam was collimated with an achromatic lens and shaped into a one-sided light sheet using a cylindrical lens. On the detection side, fluorescence collected by an objective lens passed through a motorized six-position filter wheel for automated multicolor acquisition and was directed either to a hyperspectral camera (imec SNAPSCAN-VNIR), in which a line-scan sensor is internally scanned to acquire two-dimensional spectral images[28], or to the CMOS camera through a tube-lens and a removable mirror (**Fig. 1a-c**). This dual-path design enabled both hyperspectral and CMOS-based fluorescence imaging within a single optical configuration. The optical performance of descSPIM-Galaxy was characterized by measurements of 3D images of φ1-μm fluorescent beads. Point spread function (PSF) was evaluated by fluorescence intensity profiles of single bead images, yielding lateral and axial resolutions of 7.27 ± 0.37 μm and 27.22 ± 0.69 μm, respectively (**Fig. 1d, e**). The lateral

resolution was lower than that of the descSPIM-basic full-FOV (FF) mode configuration, likely reflecting the larger camera pixel size used for hyperspectral detection (5.5 μm × 5.5 μm versus 3.45 μm × 3.45 μm of the CMOS camera), whereas the axial resolution remained comparable to that of descSPIM-basic in FF mode (lateral, 4.2 μm; axial, 26.0 μm)[24].

We evaluated the benchmark capability of volumetric spectral separation of descSPIM-Galaxy using an optical phantom composed of Protein A/G agarose beads embedded in a transparent agarose gel, each labeled with a single Alexa Fluor® dye (**Fig. 1f and Supplementary Fig. 2**). Using five excitation wavelengths, we acquired a 150-band hyperspectral dataset over a volume of 5.98 mm × 11.26 mm × 3.00 mm. The total imaging time was approximately 15.5 h, corresponding to approximately 3 h per excitation wavelength. Single-color reference spectra were used as spectral references for slice-by-slice linear spectral unmixing, enabling successful separation of 11 spectrally overlapping fluorophores across the entire three-dimensional phantom volume using only the hyperspectral camera. The unmixed fluorescence volumes were then reconstructed as three-dimensional datasets (**Supplementary Fig.2**).

To assess the utility of descSPIM-Galaxy for biological applications, we next examined the 7-color multiplex imaging for a whole cleared mouse embryo at E12.5 (**Fig. 1g**) and as single-channel views in **Supplementary Fig. 3a**. Enlarged views of representative anatomical regions are shown in **Supplementary Fig. 3b–e**. The color number was among the highest reported for single-round volumetric multiplexing of cleared sample, even though the number was reduced from the benchmark due to the substantial variability in antigen abundance, antibody accessibility, and staining efficiency. We stained multiple anatomical structures under development using anti-TAG-1 (FITC), TNNI3 (Cy3), TUBB3 (Alexa Fluor® 594), RUNX2 (Alexa Fluor® 647), αSMA (Cy5.5), CD31 (DyLight® 755) antibodies with nuclei (POPO®-

1) as a structural reference. Using the hyperspectral camera, we successfully separated four fluorophores (TNNI3 (Cy3), TUBB3 (Alexa Fluor® 594), RUNX2 (Alexa Fluor® 647), αSMA (Cy5.5)) by spectral unmixing. The failure to detect the remaining two fluorophores (TAG-1 (FITC), CD31 (DyLight® 755) was likely attributable to the limited sensitivity of the camera, preventing reliable detection of weak fluorescence signals arising from low-abundance targets. We therefore explored a hybrid imaging strategy combinationally using the hyperspectral camera and the CMOS camera with filters to increase the number of detectable channels in biological specimens (**Fig 1a, b**). The two stack images from the two different cameras were merged by cross-modal registration using nuclear staining as a common reference (See **Methods**). Registration accuracy was evaluated by correlation-based mapping and residual shift correction, supporting accurate integration of hyperspectral and CMOS-derived channels (**Supplementary Fig. 4**). A part of the registered channels were manually curated and occasionally shifted using a structural benchmark for more accurate registration (**Supplementary Fig. 5)**. The full imaged volume was 5.98 mm × 11.26 mm × 6.00 mm. Hyperspectral imaging required approximately 45 h in total, corresponding to approximately 15 h for each of the three hyperspectral acquisition channels, while CMOS-based imaging required approximately 1.5 h in total, corresponding to approximately 0.5 h for each of the three CMOS acquisition channels. The total imaging time was therefore approximately 47 h, after which the embryo region was cropped for visualization. The overall imaging, unmixing, and registration pipeline is summarized in **Supplementary Figs. 6 and 7**.

The 7-color multiplex dataset further enabled integrated visualization of spatial relationships among multiple embryonic tissues within the same whole-embryo volume. For each representative region, anatomical relationships were evaluated using both 3D renderings and corresponding 2D slice views **(Fig. 1h–j**). By comparing the TAG1 and TUBB3 channels, TAG1-positive signals were relatively enriched in the dorsal telencephalic/cortical primordium

compared with the broader TUBB3-positive neuronal signal, suggesting regionally patterned axon-associated organization in the embryonic cortex (**Fig. 1h**). By combining the TNNI3 and TUBB3 channels, TUBB3-positive neural structures were visualized around the TNNI3-positive embryonic heart, with trajectories compatible with those expected for the developing cardiac plexus (**Fig. 1i**). By integrating the RUNX2, CD31, TUBB3, and TAG1 channels, CD31-positive vascular structures and TUBB3/TAG1-positive intercostal nerves were observed in close apposition between adjacent RUNX2-positive developing ribs. In many intercostal regions, CD31-positive structures appeared superior or rostral to the neural structures, consistent with the expected spatial organization of intercostal neurovascular bundles **(Fig. 1j)**. These detailed interrogations illustrate the ability of descSPIM-Galaxy to facilitate observation-driven identification of complex 3D spatial relationships across multiple anatomical structures and molecules.

Together, these results show that descSPIM-Galaxy enables 7-color whole-embryo volumetric imaging by combining multi-wavelength excitation, dual-path detection, hyperspectral unmixing, and cross-modal image registration; because these are added to the shared descSPIM-basic core, this high-content multiplexing is realized as one interoperable configuration of the descSPIM-Advanced platform rather than a dedicated multiplexing instrument.

descSPIM-Deepsky: A high-resolution configuration for three-dimensional histology

To address the need for a higher-resolution configuration optimized for three-dimensional histology in cleared tissues, we developed descSPIM-Deepsky, extending the resolving power of descSPIM-basic. descSPIM-Deepsky was designed to improve spatial resolution and reduce stripe artifacts while maintaining a cost-effective architecture of descSPIM-basic (**Fig. 2a, b**).

To achieve this, the system includes additional components such as a galvanometer mirror, a 10×, 0.28 NA detection objective and a piezo-electric emission filter slider. Multiple components from descSPIM-basic such as the camera, light source, detection objective, and optomechanical components could be repurposed in the construction of descSPIM-Deepsky if required.

The entire descSPIM-Deepsky optical setup can be assembled on a 600 mm x 450 mm optical table and is built in a 30 mm cage system for compactness and ease of alignment (**Fig. 2c**). Light from a multi-color laser light source was coupled to a single mode fiber and collimated with an achromatic doublet. Two mirrors steer the beam through a cylindrical lens, focusing the light onto a galvanometer mirror which scans the beam in the vertical direction. The scanned light sheet is imaged by a 200-mm achromatic lens onto the back focal plane of a well-corrected 2×, 0.1 numerical aperture (NA), long-working-distance air objective, producing a pivoted light sheet at the illumination objective focal plane[11]. The entire illumination arm was constructed on a linear stage, allowing the light sheet waist to be easily translated through the sample, removing the requirement of an inner and outer immersion chamber as was the descSPIM-basic. We implemented a straight-forward method to adjust the light-sheet thickness in the sample by incorporating an adjustable slit before the cylindrical lens. Importantly, the light-sheet thickness is directly correlated with the effective FOV (eFOV): thinner light-sheets provide a smaller eFOV with improved axial resolution, while thicker light-sheets allow for a larger eFOV with reduced axial resolution (**Fig 2d; Supplementary Fig. 8a-d**). This offers flexibility in optimizing the illumination parameters for specific imaging requirements. The use of a galvanometer mirror to pivot the light sheet and reduce stripe artefacts is especially important for samples that contain opaque regions (**Supplementary Fig. 8e, f**).

On the detection side, fluorescence is collected by the detection objective lens and relayed to the camera through a tube lens, while a piezo-electric emission filter slider enables automated switching of color channels. For higher resolution imaging, we chose a 10×, 0.28 NA long working distance air objective lens for detection. In combination with a CMOS camera with 3.45 µm × 3.45 µm pixels it provides modest lateral oversampling with a field of view of 1.41 mm × 0.75 mm. For the thick light-sheet we observed an average axial full width at half maximum (FWHM) of 6.40 ± 0.58 µm (n = 11,507 beads), homogenous over the entire FOV. We therefore estimate the beam waist w_0 to be similar to the average FWHM. For the thin light-sheet, we observed a non-homogenous axial FWHM over the FOV. Therefore, we calculate the size of the usable light-sheet by measuring the FHWM of a representative bead in the middle of the FOV *(*$FWHM_{center}$ = 3.78 µm) and calculate the useable light-sheet length b as b = ($2\pi \times FWHM_{center}$^2) / λ = 171.00 µm (**Fig 2d; Supplementary Fig. 8a-d**). Assuming w_0 is equal to the $FWHM_{center}$, the usable light-sheet is therefore approximately 22.7% of the full FOV (FOV_x = 745.2 µm). Within the cropped FOV, we measured an average axial FWHM of 4.06 ± 0.43 µm (*n* = 4,092 beads). Along the lateral dimension, the FWHM was similar between the thick and thin light-sheet, on average 1.09 µm (*n* = 15,149 beads) (**Fig. 2e; Supplementary Fig. S9a-d**).

For biomedical applications of descSPIM-Deepsky, we first performed imaging of cleared rat embryonic kidneys stained with Alexa Fluor® 555 NHS ester and propidium iodide. Volumetric imaging of samples larger than the microscope's FOV was achieved by sample tiling and stitching. As the illumination arm was constructed on a linear stage, the light-sheet waist could be easily translated through the sample, thereby facilitating tiled imaging with improved axial resolution **(Fig. 2f, g**). The datasets were acquired in 65 minutes. The cellular architecture of the kidney could be observed (**Fig. 2h**) and, in the axial plane, nuclei could be clearly differentiated (**Fig. 2i**). The acquired images were computationally rendered as false-

color H&E-like images using FalseColor-Python[29], allowing a high-resolution histopathological evaluation (**Fig. 2j**).

We further demonstrated a high-resolution volumetric imaging of a cleared mouse lung stained with propidium iodide, Atto594 NHS ester, and anti-GFP nanobodies marking surfactant associated protein C (Sftpc) expressing alveolar epithelial type II cells[30](Fig. 2k). The acquisition of all channels was completed in 94 minutes. The high resolution, high signal-to-noise ratio 3D image allowed us to quantify the spatial distribution of GFP-positive type II cells by automated detection with a commercially available image analysis software (Imaris). We measured 887 cells in 8.366×10^7 μm^3 （10602 cells/mm^3） of the tissue, with an accuracy > 99% (**Supplementary Fig. 9**). The uniform spatial distribution of this sparse cell type could be precisely quantified from the representative 3D data.

These results show that descSPIM-Deepsky brings subcellular-scale, three-dimensional histology of cleared specimens into the descSPIM-Advanced platform by augmenting descSPIM-basic with high-resolution detection optics and light-sheet pivoting, without requiring a separate high-resolution microscope.

descSPIM-Fullmoon: A large-field configuration for organ-scale imaging

To address the need for larger sample imaging without tiling, registration, or stitching, we developed descSPIM-Fullmoon as a wide-field configuration, adding the capability of organ-scale imaging to descSPIM-basic. descSPIM-Fullmoon was developed by introducing a large-format telecentric lens and a large-size sensor camera into the detection path of descSPIM-basic, while incorporating dual-sided light-sheet illumination and galvanometer mirror-mediated light-sheet pivoting into the illumination path (**Fig. 3a-c)**. The system was assembled on a 300 mm × 450 mm optical breadboard (**Fig. 3b, c**). Single-mode fiber-coupled laser light was collimated with an achromatic convex lens (f = 100 mm). The dual-sided light-sheet

illumination was adopted to avoid the attenuation of image quality at the deeper area from the illumination side of a cleared large specimen. The excitation beam was thus split into two illumination paths by a 50:50 beam splitter cube, thereby enabling the use of the laser light source from descSPIM-basic. Each path was then shaped into a light sheet using a cylindrical lens (f = 500 mm) as in descSPIM-basic. The excitation beam passed through a slit and a galvanometer mirror, and then through a cylindrical-lens beam expander composed of f = 30 mm and f = 130 mm plano convex lenses, enabling both beam expansion and light-sheet pivoting. The detection path consisted of a 2-inch filter, a 1× large-format telecentric lens, and a CMOS camera with a sensor size of 23.8 mm × 35.8 mm (3.76 µm × 3.76 µm pixel size).

PSFs were evaluated using the FWHM of fluorescent intensity profiles from 3D images of Φ1-µm fluorescent beads. The lateral resolution at the center of FOV was unaffected by galvanometer mirror-mediated light-sheet pivoting (off, 5.22 ± 0.06 µm; on, 4.99 ± 0.06 µm (**Fig. 3d and Supplementary Fig. 10a**). In contrast, the axial resolution deteriorated about 28% from 33.8 ± 0.53 µm with the galvanometer mirror turned off to 43.3 ± 1.23 µm with the galvanometer mirror turned on at the center of FOV (**Fig. 3e and Supplementary Fig. 10a**). Although the axial resolution was 1.66 times lower than that of descSPIM-basic (26.0 µm in FF mode), it provided a uniform light-sheet illumination (twice the Rayleigh length: 25.2 mm without light-sheet pivoting; 50.7 mm with light-sheet pivoting) that can cover the entire CMOS sensor width (23.8 mm, **Fig. 3f and Supplementary Fig. 10a**). However, when a 20-mm-wide glass cuvette was used, the x width of the FOV was limited to 19.8 mm (**Fig. 3f and Supplementary Fig. 10a**). Pivotting slightly reduced fluorescence intensity at the upper and lower edges of the y axis of the FOV (28.1 mm). Thus, the eFOV of the setup shown here was 19.8 mm × 28.1 mm, while the area was still sufficient for a cm-order of whole large specimens (**Fig. 3f and Supplementary Fig. 10a**). The lateral FWHM values were stable across the eFOV

while the axial FWHM increased slightly toward the lateral edges of the eFOV (up to 1.10-fold without light-sheet pivoting and 1.20-fold with light-sheet pivoting).

This enables single-field capture of a whole mouse brain stained with SYTOX® Green volumetrically expanded approximately tenfold with CUBIC-X[31] without requiring tiling, registration, or stitching (**Fig. 3f**). The expanded whole mouse brains were scanned within 4 minutes per channel using descSPIM-Fullmoon. The data size after region of interest (ROI) cropping was approximately 20 gigabytes per channel, which did not require a high-performance computational environment for image processing (see **Methods**).

The simultaneous dual-sided illumination compensated for attenuation of excitation light across large specimens, and light-sheet pivoting effectively reduced stripe-like shadow artifacts, enabling uniform imaging of cleared large tissues such as rat brain coronal sections stained with SYTOX® Green without image-processing-based destriping (**Fig. 3g**). Furthermore, descSPIM-Fullmoon also supports multicolor imaging of an expanded whole mouse brain triple-stained with nucleus (SYTOX® Green), tryptophan hydroxylase 2 (Tph2, Cy3), and tyrosine hydroxylase (Th, Alexa Fluor® 647) by utilizing multi-track acquisition (acquisition time was 2.79 min per channel, **Fig. 3h and Supplementary Fig. 10b–f**). In *x*-*z* images, Tph2-labeled single cells were sufficiently resolved although a degree of elongation was observed (**Supplementary Fig. 10f**). Exploiting the enhanced resolving capability of ExM, we quantitatively counted Tph2-positive cells throughout the brain and identified a total of 7,581 cells.

Together, by extending the same descSPIM-basic core with large-format detection and dual-sided pivoted illumination, descSPIM-Fullmoon brings organ-scale, single-field imaging into the descSPIM-Advanced platform, so that whole-organ coverage and the finer-scale capabilities above coexist as configurations of one system and open opportunities for organ- and body-wide screening.

descSPIM-SLIM: A simpler and more affordable system for cleared tissue imaging

To enhance the opportunity of routine cleared tissue imaging, we developed descSPIM-SLIM, a further simplified and affordable light-sheet configuration from descSPIM-basic (**Fig. 4**). To suppress costs, we adopted compact laser-diode modules emitting at 405, 520, and 639 nm with an output power of 4.5 mW each as the excitation light sources. Laser-diode modules provide pre-collimated, single spatial mode laser beams in a small plug-and-play format, allowing the illumination path to be assembled without fiber coupling or an external laser combiner. In descSPIM-SLIM, a single-sided light sheet is generated using a 10× beam expander followed by a cylindrical lens (f = 100 mm). A tunable slit placed before the cylindrical lens adjusts the effective excitation NA and light-sheet thickness (**Fig. 4a**). This approach omits the need to install long-working-distance cylindrical lenses, as in descSPIM-basic, thereby shortening the excitation optical path. On the detection side, unlike the other variants, an inverted configuration with the objective lens positioned below the sample made the system more compact. Fluorescence is collected through a 2× objective lens mounted on an electronically driven z stage and relayed to a CMOS camera through a right-angle kinematic mirror, a filter and a tube lens (f = 100 mm), yielding an effective total magnification of 1× and a sampling of 3.45 μm per pixel at the imaging plane (**Fig. 4a**). This optical layout provides a compact and rapidly deployable LSFM configuration for cleared-tissue imaging, with all optical components fitting on a 200 mm × 250 mm breadboard and requires only a few hours for assembly (**Fig. 4b, c**).

We evaluated the optical performance of descSPIM-SLIM by PSF analysis using φ1-μm fluorescent beads under different slit-width settings (**Fig. 4d, e**). Lateral resolutions were comparable between slit widths, with values of 4.42 ± 0.23 μm at a 6-mm slit width and 4.43

± 0.32 μm at a 3-mm slit width. In contrast, axial resolution varied with the slit setting, measuring 6.68 ± 0.34 μm at a 6-mm slit width and 11.62 ± 0.37 μm at a 3-mm slit width. These results show that the adjustable slit enables control of light-sheet performance while maintaining a lateral resolution comparable to the previously reported values for descSPIM-basic in FF and FA modes (4.2 and 4.4 μm, respectively)[24].

Finally, we used descSPIM-SLIM for multicolor volumetric imaging application of cleared E12.5 mouse embryos (**Fig. 4f, g**). Using the laser-diode modules as excitation light sources, descSPIM-SLIM enabled three-color whole-embryo imaging with a 3D cellular resolution (**Fig. 4f**).

We also tested an alternative excitation configuration in which the laser-diode module was replaced by a single-mode fiber-coupled multi-line laser beam combiner. In this configuration, the aspheric lens was removed, and the output end of the single-mode fiber was positioned at the focal position of an f = 100 mm collimating lens, allowing four excitation wavelengths, 405, 488, 561 and 640 nm, to be introduced into the SLIM illumination path. PSF analysis showed that the fiber-coupled laser-light-source configuration resulted in an inferior axial resolution than the laser-diode-module configuration at the same 6-mm slit setting, with axial resolutions of 10.69 μm and 6.68 μm, respectively (**Fig. 4e and Supplementary Fig. 11**). This slight deterioration of the axial resolution is likely attributable to the difference of incident beam profile to the cylindrical lens; the directly collimated single-mode-fiber output may provide a steeper Gaussian beam profile than the compact laser-diode modules, reducing effective excitation NA. However, by taking advantage of the increased color channel numbers of this fiber-coupled configuration, we successfully obtained a four-color volumetric image of a cleared E12.5 mouse embryo labelled with CD31 (FITC), TUBB3 (Alexa Fluor® 594), αSMA (Alexa Fluor® 647), and nuclear staining (POPO®-1) (**Fig. 4g**). The image quality was

sufficient to evaluate the distributions of labeled structures across the whole body, ensuring its routine use for various biological applications. For the representative embryo datasets, image acquisition required approximately 1.8 min per channel, corresponding to total acquisition times of approximately 5.5 min for the three-color dataset and 7.3 min for the four-color dataset, excluding channel-switching and handling overheads.

Together, these results show that descSPIM-SLIM supports three-color whole-embryo-scale imaging with an affordable laser-diode-module configuration that can be assembled for approximately US$15,000, and expands to four-color imaging through a fiber-coupled excitation option; by reducing the shared core to its simplest, lowest-cost form while remaining part of the descSPIM-Advanced platform, SLIM lets laboratories enter at minimal cost and later reconfigure or upgrade toward the higher-performance variants.

Building a unified operation platform of descSPIM-Advanced

To integrate all the descSPIM devices into a single ecosystem, we finally developed the Mission Control Center (MCC), a unified graphical user interface (GUI) software (**Fig. 5a**). MCC coordinates the electronic devices and imaging workflows shared across the platform including cameras, sample stages, camera stages, laser light sources, filter wheels, galvanometer mirrors and other motorized components as predefined workflows that support automated multi-color and multi-stack acquisitions (**Fig. 5b**). MCC employs a modular backend in which device-specific control functions are implemented as independent modules, so that additional hardware can be incorporated by adding the corresponding backend modules without modifying the core software. As an exception, hyperspectral acquisition is handled through a dedicated GUI in descSPIM-Galaxy, because the internal-scanning workflow of the hyperspectral camera differs from conventional frame-based control[28]. Therefore, the hyperspectral camera is independently coordinated with the sample stage, camera stage, filter

wheel and laser light sources, while the remaining device-control functions are organized within the common MCC framework. We demonstrated that all the descSPIM variants can be controlled by the single device control software (**Fig. 5c**).

In the ecosystem, all four variants were designed as modular extensions of descSPIM-basic[24] (**Fig. 6a**), while maintaining compatibility with its common design framework, allowing users to customize and upgrade their systems according to laboratory-level research requirements. Despite these variant-specific customizations, platform-wide interoperability was retained. Detailed construction manuals, parts lists, imaging protocols, sample-preparation workflows and MCC installation and operation instructions for all models are openly available through the descSPIM-Advanced GitHub repository (https://github.com/dbsb-juntendo/descSPIM-Advanced). To date, the descSPIM platform has been deployed at 58 laboratories worldwide (**Fig. 6b**).

Discussion

The widespread adoption of descSPIM-basic, an affordable LSFM, has accelerated routine cleared-tissue imaging and revealed additional needs that cannot be met with current hardware. To address these needs, we developed descSPIM-Advanced, an ecosystem in which high-end capabilities coexist as interoperable, off-the-shelf variants rather than specialized independent instruments. As a result, capabilities that previously required individual dedicated systems, such as high multiplexing, subcellular resolution, organ-scale fields of view and low-cost routine imaging can now be accessed and reconfigured within one platform at the laboratory-level.

This positions descSPIM-Advanced as a complementary, laboratory-level counterpart to commercial and facility-level LSFM systems. Commercial systems provide high imaging performance and operational stability through complex, versatile functionality, but their high cost keeps them beyond the reach of many individual laboratories. Community-driven systems such as the mesoSPIM initiative have expanded access, yet many advanced functions still demand substantial optical expertise and custom implementation[19,20], making them better suited to facility-level deployment. More recent off-the-shelf high-performance systems have further extended accessible LSFM, but each still delivers only a specialized capability as a dedicated instrument[25,26]. descSPIM-Advanced fills this gap by consolidating multiple capabilities on one accessible platform, so that a laboratory can perform routine cleared-tissue imaging for evaluating clearing, staining and imaging conditions. When greater performance is required, the systems can be reconfigured or upgraded to a purpose-optimized variant in-house, while facility-level systems remain complementary for analyses beyond its scope. This division of roles may broaden the practical dissemination of cleared-tissue LSFM.

descSPIM-Galaxy incorporates hyperspectral imaging to resolve up to 11 fluorescence channels in a single acquisition, extending accessible cleared-tissue LSFM into multispectral imaging, which requires both broad excitation/emission coverage and separation of spectrally overlapping signals[27]. Building on prior hyperspectral LSFM approaches[32,33,34,35,36,37], Galaxy provides a practical descSPIM-based workflow integrating multi-wavelength excitation, hyperspectral detection[28], spectral unmixing and cross-detector integration, enabling separation of up to 11 channels in a single specimen without iterative multi-round staining. Galaxy may also make cyclic multiplexing more practical for volumetric cleared tissues[38,39,40]: an 11-color implementation could reduce the imaging rounds needed for a given panel by roughly threefold relative to conventional three- to four-channel systems, supporting future organ-wide spatial molecular profiling and cellomics[3,27,41,42]. Deepsky and Fullmoon provide complementary solutions to the most frequently requested user demands for higher resolution and larger, organ-scale acquisition within reach of individual laboratories. Deepsky achieves subcellular resolution, enabling false-colored, high-resolution histology and single-cell-level quantitative annotation of cellular distributions in three dimensions, whereas Fullmoon enables single-field, organ-scale imaging even after tissue expansion, without tiling, registration or stitching, making it well suited to routine whole-organ and whole-body 3D imaging. Finally, SLIM can be assembled for approximately USD 15,000 with a low-cost three-wavelength source, providing a practical entry point for routine three-color imaging.

Mission Control Center (MCC) provides the shared operational layer of the ecosystem, coordinating the cameras, sample and camera stages, laser light sources, filter changers and galvanometer mirrors used across descSPIM-basic and all variants. Whereas general control platforms such as μManager and ImSwitch offer broad flexibility but require custom scripting or device-specific configuration for coordinated operation[43,44,45], and our earlier descSPIM-basic program still relied on external control boards and technical expertise[24,43,44], MCC

exposes descSPIM-family operations as predefined workflows for automated multi-color, multi-stack acquisition. Its modular backend allows new hardware to be added as independent modules without altering the core software, facilitating future expansion of the ecosystem.

Current descSPIM-Advanced systems do not remove the technical constraints inherent to cleared-tissue LSFM: effective operation still requires basic optical-alignment, device-control and sample-handling knowledge, and image quality depends on clearing efficiency, refractive-index matching, labeling quality and residual pigmentation. Each variant also retains trade-offs. Galaxy requires careful fluorophore selection, single-color reference acquisition, longer acquisition and larger datasets. Deepsky trades FOV for resolution and needs precise alignment. Fullmoon trades axial resolution for coverage. And SLIM may require a higher-power fiber-coupled source for weakly labeled specimens or high-power imaging. As an open, modular platform, deployment also depends on device availability, software maintenance, data-processing infrastructure and appropriate safety management for lasers and clearing reagents. Future advances in camera sensitivity, acquisition strategies and accelerated data-processing pipelines may further improve throughput and usability.

Despite these limitations, descSPIM-Advanced provides a scalable framework for extending cleared-tissue LSFM from routine toward application-specific advanced imaging in individual laboratories. Its significance lies not only in the performance of the individual variants but in the platform concept itself: laboratories can select, build, customize and upgrade configurations according to their biological questions, budget and technical readiness. By extending the democratizing concept of descSPIM-basic from access to a single affordable microscope toward access to a family of customizable, interoperable configurations, descSPIM-Advanced may broaden the practical use of cleared tissue imaging in 3D spatial biology across diverse biological laboratories.

Methods

Construction of descSPIM-Advanced variants

All parts list and detailed information on the construction and usage of descSPIM-Advanced are opened in our GitHub website (https://github.com/dbsb-juntendo/descSPIM-Advanced).

descSPIM-Galaxy

In brief, the descSPIM-Galaxy system was constructed on a 300 mm × 450 mm optical breadboard (MB3045/M, Thorlabs, Newton, NJ, USA). The system consisted of an illumination arm, a detection arm, and a sample-positioning stage. For the excitation arm, excitation light was supplied by two-kinds of multi-line laser beam combiners (Cobolt Skyra; 488, 515, 561, and 647 nm, HÜBNER Photonics, Solna, Sweden and Cobolt C-FLEX; 405 and 730 nm, HÜBNER Photonics). The two fiber-coupled inputs, of which polarization directions are perpendicular each other, were combined using a polarizing beamsplitter cube (CCM1-PBS251/M, Thorlabs), collimated with an achromatic lens (AC254-100-A, Thorlabs) and directed to the cylindrical lens (f = 500.0 mm, LJ1144RM-A, Thorlabs). Before the cube, beam orientations of two-kinds of fiber-coupled excitation lights were adjusted by SM1-to-fiber adapter modules (SM1FCA, Thorlabs) mounted in XY-adjustable holders (CXY1A, Thorlabs). The combined beam was then focused by the cylindrical lens (f = 500.0 mm, LJ1144RM-A, Thorlabs) to be coincided with the central position of sapmles along the optical axis of the detection arm. The detection arm incorporated a 1× objective lens (TL1X-SAP, Thorlabs), a motorized filter wheel (FW103/M, Thorlabs) loaded with wavelength-matched long-pass or band-pass filters, a tube lens (f = 200 mm, TTL200-A, Thorlabs), and a removable mirror (DFM1/M, Thorlabs) to select the emission path toward a hyperspectral camera (SNAPSCAN VNIR, imec, Leuven, Belgium) or a CMOS camera (CS895MU, Thorlabs). The

filter wheel included a 425 nm long-pass filter (#84-742, Edmund Optics, Barrington, NJ, USA), a 520/40 nm band-pass filter (FBH520-40, Thorlabs), a 575 nm long-pass filter (#84-745, Edmund Optics), a 675 nm long-pass filter (#84-747, Edmund Optics), and a 750 nm long-pass filter (FELH0750, Thorlabs). The detection module was mounted on optical rails (RLA150/M, Thorlabs) attached to a motorized camera stage (XR25P/M with Z825B actuator, Thorlabs). The sample-positioning stage was also attached with a motorized actuator (Z825B, Thorlabs) along the optical axis of detection arm (*z*-axis) . For synchronization between stage motion and camera exposure was implemented through TTL triggering. Optical alignment was performed according to the descSPIM-basic alignment procedure, which is publicly available through the descSPIM GitHub repository (https://github.com/dbsb-juntendo/descSPIM)[24].

To align the two-kinds of laser beams from laser beam combiners, the 405 nm and 488 nm lights were used for imaging of dual-color fluorescent agarose beads prepared by labeling Protein A/G PLUS–agarose beads (15 µL settled volume, Santa Cruz Biotechnology, Dallas, TX, USA) with Goat anti-Mouse IgG (H+L) Cross-Adsorbed, Alexa Fluor® 405 (A-31553, Invitrogen, Carlsbad, CA, USA) and Donkey anti-Goat IgG (H+L) Highly Cross-Adsorbed, Alexa Fluor® 488 (A-11055, Invitrogen). Image stacks were acquired with the CMOS camera under 405 nm and 488 nm excitation, merged in Fiji/ImageJ[46], and inspected in orthogonal views to evaluate axial and lateral offsets between the two excitation paths. When residual misalignment was observed, the excitation path was adjusted using the XY translator (CXY1A, Thorlabs), and image acquisition was repeated until the two images were matched in pixel level position (**Supplementary Fig. 1**).

Image acquisition and microscope control for descSPIM-Galaxy were performed using an Endeavor Pro9100 desktop workstation (Epson Direct Corp., Nagano, Japan) equipped with an Intel Core i9-10900X processor (10 cores, 3.7 GHz), 64 GB DDR4 RAM, and a 16-TB

IronWolf HDD (ST16000VN001; CMR, SATA 6 Gb/s, 7,200 rpm; Seagate Technology LLC, Fremont, CA, USA) mounted in a 5.25-inch trayless SATA mobile rack (HSB100SATBK; StarTech.com Ltd., London, ON, Canada), running Windows 10 Pro 64-bit.

descSPIM-Deepsky

The descSPIM-Deepsky system was constructed on a 450 mm × 600 mm optical breadboard (MB4560/M, Thorlabs). The system consisted of an illumination arm, a detection arm, and a sample-positioning stage mounted on independent translation assemblies. The illumination arm was incorporated into a 30-mm cage system for compactness and was placed on two manual translation stages (Thorlabs, XR25/M) to axially move the light-sheet focus. A 4-color multi-line (405, 488, 532, 641 nm) Cobolt Skyra was used as a light source and was coupled into a single-mode fiber and collimated using a 50 mm achromatic lens (AC254-050-A, Thorlabs). The size of the beam along the horizontal dimension was controlled using an adjustable slit (VA100/M, Thorlabs) and the resulting beam was steered with two mirrors onto the cylindrical lens (f = 50 mm, ACY254-050-A, Thorlabs) which created a focused beam along one dimension onto a galvanometer mirror (GVS211/M, Thorlabs). The scanning mirror was operated in 1 deg/Vmode at 2 V and 200 Hz with a common waveform generator (DG822, RIGOL Technologies, Suzhou, ChinaRigol). The resulting scanned beams were de-scanned by a long focal length achromatic lens (f = 200 mm, AC254-200-A, Thorlabs) and projected onto the back focal plane of the illumination objective (TL2X-SAP, Thorlabs) which created the light-sheet in the sample. The detection arm was built on a motorized crossed-roller translation stage (XR25P/M with Z825B actuator, Thorlabs) and incorporated a 10× objective lens (MY10X-803, Thorlabs), a filter slider (ELL9, Thorlabs), a tube lens (TTL200-A, Thorlabs; f = 200 mm), and a CMOS camera (CS895MU, Thorlabs). The detection arm was assembled using dovetail rails, rail carriages, posts, cage plates, thread adapters and lens tubes. The

sample-positioning stage consisted of a motorized crossed-roller translation stage (XR25P/M with Z825B actuator, Thorlabs), a dovetail rail (XR25DR2, Thorlabs), and a self-contained XYZ translation stage (LX30/M, Thorlabs). A cuvette support was formed using a mounting base (BA1/M, Thorlabs) and a microscope slide spring clip (SLH1/M, Thorlabs) attached through an AE4M6MS adapter (Thorlabs). The microscope control and image visualization and processing were performed on a Windows 11 workstation with an Intel Xeon E-2286M CPU, 64 GB of RAM and a NVIDIA GeForce RTX 2060 graphics card.

descSPIM-Fullmoon

The descSPIM-Fullmoon system was constructed on a 300 mm × 450 mm optical breadboard (MB3045/M, Thorlabs). Excitation light was provided by a fiber-coupled laser combiner (488, 561, and 647 nm, 50 mW each, Cobolt Skyra). A fiber-coupled beam was collimated using an achromatic lens (AC254-100-A, Thorlabs) mounted in an XY translating lens mount (CXY1, Thorlabs), and then split into dual-sided illumination paths by a 50:50 beam splitter (CCM1-BS013/M, Thorlabs). Each illumination arm contained a cylindrical lens for light-sheet formation (f = 500 mm, LJ1144RM-A, Thorlabs), the galvanometer mirror (GVS001, Thorlabs), a cylindrical beam expander (LJ1212L1-A and LJ1640L1-A, Thorlabs), and a 2-inch mirror. The galvanometer mirror was operated in 0.8 deg/V mode at 8 V and 80 Hz with a common waveform generator (JDS6600, Joy-IT, Neukirchen-Vluyn, Germany). The detection arm consisted of a large-size CMOS sensor (DS50M, Nikon, Tokyo, Japan) coupled to a large-format telecentric lens (LSTL10H-F, Myutron, Tokyo, Japan) through a 2-inch filter holder (LCFH2/M, Thorlabs) and associated adapters (K&F CONCEPT, Shenzhen, China). The detection optics was mounted on a motorized translation stage (XR25P/M with Z825B actuator, Thorlabs) via a holder (VC3C/M, thorlabs) on a rail (XT66SD-250, thorlabs) and carriage (XT66P2/M, Thorlabs). The sample-positioning stage was assembled from a

translation stage (XR25P/M, Thorlabs) on a rail (XR25DR2, Thorlabs), a construction rail (XT66-100, Thorlabs), a motorized translation stage (XR25P/M with Z825B actuator, Thorlabs), a vertical translation stage (MVS05/M, Thorlabs), rails (RLA150/M, Thorlabs), and a rotation stage (PR01/M, Thorlabs).

Image acquisition and microscope control were performed using a desktop computer running Windows 11 (Microsoft) equipped with an Intel Core i9 (14900K) processor, 224 GB RAM, and an NVIDIA RTX A4000 graphics card. Image processing and visualization were performed on the same computer unless otherwise stated.

descSPIM-SLIM

The descSPIM-SLIM system was constructed on a 200 mm × 250 mm optical breadboard (MB2025/M, Thorlabs). Excitation lights were provided by USB-connected compact laser diode modules (405, 520, 639 nm, 4.5 mW each; PL255, PL251 and PL252, Thorlabs), and introduced into the illumination arm via a kinematic adapter (KAD11F, Thorlabs). The beam was expanded using a beam expander consisting of an aspheric lens (f = 11 mm, C061TMD-A, Thorlabs) and an achromatic doublet lens (f = 100 mm, AC254-100-A-ML, Thorlabs). For the fiber-coupled configuration, single-mode-fiber-coupled laser lights (405, 488, 561, and 640 nm, 25 mW each, iChrome CLE laser combiner, TOPTICA Photonics, Gräfelfing, Germany) were collimated with the f = 100 mm collimating lens. The collimated light was shaped into a light sheet using a cylindrical lens (f = 100 mm, ACY254-100-A, Thorlabs). The variable slit (VA100CP/M, Thorlabs) was placed upstream of the cylindrical lens to control the effective illumination NA and FOV. The detection arm consisted of a 2× objective lens (TLX2X-SAP, Thorlabs), an emission filter holder (SM1QP, Thorlabs), a tube lens (TTL100-A, Thorlabs; f = 100 mm), and a CMOS camera (LP162MU, Thorlabs), yielding an overall magnification of 1×. The optical axis of the objective lens was folded vertically to the bread board. Fluorescent

lights were collected by the objective lens and then reflected by a single mirror in a right-angle kinematic mirror mount (KCB1EC/M, Thorlabs) to the tube lens and CMOS camera via accommodate emission filters horizontally aligned on the breadboard. The detection objective was mounted on a motorized translation stage (CTB1B/M with ZF25B actuator, Thorlabs) for axial positioning. Samples were mounted in transparent cuvettes on a holder composed of crossed-roller translation stages (XR25P/M, Thorlabs), with one axis motorized using a ZST225B actuator (Thorlabs).

Image acquisition and microscope control for descSPIM-SLIM were performed using a raytrek R5-RL5 mobile workstation (Third Wave Corp., Tokyo, Japan) equipped with an Intel Core i7 processor (14 cores and 20 threads).

Optical characterization and resolution analysis

Optical phantom preparation

To perform the PSF evaluations, fluorescent microspheres (1:20,000–1:50,000, 1 μm diameter; Nile Red–labeled FluoSpheres, Invitrogen, Waltham, MA, USA) or multi-color fluorescent beads (1:500, TetraSpeck, 200 nm, Thermo Fisher Scientific, Waltham, MA, USA) were diluted in CUBIC-R+ containing 2% agarose and embedded loaded into a transparent 10-mm-wide glass cuvette (UG-204, Portmann Instruments, Biel-Benken, Switzerland) or 20-mm-wide glass cuvette (0309150106, Tokyo Garasu Kikai, Tokyo, Japan).

Point spread function (PSF) evaluation

PSF were evaluated using a common protocol across all descSPIM configurations. Three-dimensional image stacks of an isolated single fluorescent bead were acquired under the corresponding imaging conditions. Lateral and axial intensity profiles were extracted from individual bead images, and FWHM values were estimated by Gaussian fitting to quantify

spatial resolutions. For each condition, independent beads were analyzed (n = 10), and the results were reported as mean ± SD. Measurements were repeated in multiple independent experiments, and representative datasets were used for quantitative analysis. Representative values were calculated from the smallest measured FWHM values to minimize the effects of overlapping signals from multiple beads.

Sample preparation and data acquisition

Eleven-color fluorescent bead optical phantom

To validate multicolor hyperspectral imaging and spectral unmixing in descSPIM-Galaxy, an 11-color fluorescent bead optical phantom was prepared using Protein A/G PLUS–agarose beads conjugated with fluorophore-labelled secondary antibodies. Protein A/G PLUS–agarose beads (15 μL settled volume; Santa Cruz Biotechnology, Dallas, TX, USA) were mixed with the following fluorophore-conjugated antibodies: Goat anti-Mouse IgG (H+L) Cross-Adsorbed, Alexa Fluor® 405 (A-31553, Invitrogen); Donkey anti-Goat IgG (H+L) Highly Cross-Adsorbed, Alexa Fluor® 488 (A-11055, Invitrogen); Goat anti-Mouse IgG (H+L) Cross-Adsorbed, Alexa Fluor® 514 (A-31555, Invitrogen); Goat anti-Mouse IgG (H+L) Cross-Adsorbed, Alexa Fluor® 568 (A-11004, Invitrogen); Donkey anti-Goat IgG (H+L) Highly Cross-Adsorbed, Alexa Fluor® 594 (A-11058, Invitrogen); Goat anti-Mouse IgG (H+L) Highly Cross-Adsorbed, Alexa Fluor® 633 (A-21052, Invitrogen); Donkey anti-Rabbit IgG (H+L), Alexa Fluor® 647, minimal cross-reactivity (711-605-152, Jackson ImmunoResearch, West Grove, PA, USA); Goat anti-Mouse IgG (H+L) Cross-Adsorbed, Alexa Fluor® 660 (A-21054, Invitrogen); Goat anti-Mouse IgG (H+L) Cross-Adsorbed, Alexa Fluor® 700 (A-21036, Invitrogen); Goat anti-Mouse IgG (H+L) Cross-Adsorbed, Alexa Fluor® 750 (A-21037, Invitrogen); and Goat anti-Mouse IgG (H+L) Cross-Adsorbed, Alexa Fluor® 790 (A11375,

Invitrogen). Each antibody was used at 4–6 µg. The reaction volume was adjusted to 40 µL with PBS, and the mixture was incubated at 4 °C for 16 h. After labelling, the beads were washed three times with PBS by centrifugation for 1 min each to remove unbound antibodies.

Labelled beads were uniformly suspended in 1% (w/v) agarose in PBS and loaded into a four-sided transparent cuvette (inner dimensions, 10 mm × 10 mm × 46 mm). To generate a layered phantom, each single-color bead suspension was sequentially added at approximately 70 µL per layer, corresponding to an approximately 0.7-mm layer height within the 10 mm × 10 mm cuvette cross-section. The resulting 11-color phantom had a total z thickness of approximately 10 mm. The single-color layers were stacked in the following order from top to bottom: Alexa Fluor® 405, Alexa Fluor® 647, Alexa Fluor® 488, Alexa Fluor® 660, Alexa Fluor® 514, Alexa Fluor® 700, Alexa Fluor® 568, Alexa Fluor® 750, Alexa Fluor® 594, Alexa Fluor® 790 and Alexa Fluor® 633.

The phantom was imaged using descSPIM-Galaxy following the hyperspectral imaging workflow (**Supplementary Fig. 12a**). Hyperspectral image stacks were acquired at 50 µm z-steps over 60 slices, corresponding to a total depth of 3.0 mm, with 300 ms exposure per frame. Fluorescence was detected using long-pass filters matched to each excitation condition: 425 nm for 405 nm excitation, 500 nm for 488 nm excitation, 575 nm for 561 nm excitation, 675 nm for 647 nm excitation and 750 nm for 730 nm excitation. Excitation wavelengths were applied sequentially in the order 730, 647, 561, 488 and 405 nm. Hyperspectral detection was performed using an imec SNAPSCAN VNIR camera covering 470–900 nm with a spectral sampling interval of approximately 2.1 nm per pixel and up to 150 bands.

Animal ethics

All animal procedures were conducted in accordance with relevant institutional, national and international guidelines and regulations. Animal experiments performed at Juntendo University

were approved by the Institutional Animal Care and Use Committee of Juntendo University (approval nos. 2025248 and 2026291) and were conducted in accordance with institutional regulations and the Japanese Act on Welfare and Management of Animals. Experimental procedures performed at Kagoshima University were approved by the President of Kagoshima University after review by the Institutional Animal Care and Use Committee of Kagoshima University (permission no. VM24025). Laboratory animal care and use at Kagoshima University were conducted in accordance with the AAALAC International-accredited program of the Experimental Animal Center of Kagoshima University. Mouse and rat experiments performed in Sweden were conducted in accordance with Swedish animal welfare legislation and were approved by the Northern Stockholm Animal Ethics Committee (ethical permit no. 15598-2023 and 2645-2021).

Mouse embryo preparation and imaging

Timed-pregnant ICR mice (Slc:ICR, Japan SLC, Shizuoka, Japan) at gestational day 12 were purchased. Pregnant mice were euthanized by CO_2 inhalation, and E12.5 embryos were collected by laparotomy. Embryos were immersion-fixed in 4% PFA in PBS at 4 °C for 24 h and washed three times in PBS. After PBS wash, samples were immersed in 50% CUBIC-L (T3740, Tokyo Chemical Industry, Tokyo, Japan) for 1 h and 100% CUBIC-L for 24 h at room temperature, followed by treatment with 3% hydrogen peroxide containing 150 mM NaCl at 37 °C for 48 h[47]. Staining was performed using CUBIC-HistoVision 2.0 with HV-Additive (1.5%, #0854)[48]. Embryos were pre-incubated overnight in 5% methanol in PBS (21915-93, Nacalai Tesque, Kyoto, Japan) at 37 °C, incubated in HEPES-TSC buffer for 1 h at 37 °C, transferred into 2 mL round-bottom cryo vials (121263, Greiner Bio-One, Kremsmünster, Austria), and stained in 100 µL of staining solution. Samples were incubated for 3 d at room temperature and 1 d at 4 °C, washed three times in HEPES-TS, post-fixed in 1% formaldehyde

in HEPES-TS, and washed three times in PBS for 1 h at room temperature. Samples were then immersed in 50% CUBIC-R+ for 24 h and 100% CUBIC-R+ for 24 h at room temperature. Samples were embedded in 2% agarose (01163-76, Nacalai Tesque) dissolved in CUBIC-R+[47].

For Galaxy imaging, samples were stained in a total volume of 100 µL with POPO®-1 (60 µM; 40093, Biotium, Fremont, CA, USA) and six directly labeled primary antibodies, each at a final concentration of approximately 20 µg/mL. The antibodies comprised TAG-1 (AF4439, R&D Systems, Minneapolis, MN, USA) labeled with FITC using a Lightning-Link® Conjugation Kit (ab102884, Abcam, Cambridge, UK), TNNI3 (ab56357, Abcam) labeled with Cy3 using a Lightning-Link® Conjugation Kit (Fast) (ab188287, Abcam), TUBB3 (MMS-435P, Covance, Princeton, NJ, USA) labeled with Alexa Fluor® 594 using a Lightning-Link® Conjugation Kit (Fast) (ab269822, Abcam), RUNX2 (ab192256, Abcam) labeled with Alexa Fluor® 647 using a Lightning-Link® Conjugation Kit (Fast) (ab269823, Abcam), α-SMA (A5228, Sigma-Aldrich, St. Louis, MO, USA) labeled with Cy5.5 using a Lightning-Link® Conjugation Kit (Fast) (ab269891, Abcam), and CD31 (AF3628, R&D Systems) labeled with DyLight® 755 using a Lightning-Link® Conjugation Kit (ab269890, Abcam). Before labeling, antibody solutions were adjusted to approximately 1.0 mg/mL, when necessary, using Amicon® Ultra centrifugal filters with a 30-kDa molecular-weight cutoff (Millipore, Burlington, MA, USA), and conjugation was performed according to the manufacturers' instructions. Samples were embedded in CUBIC-R+ agarose inside four-sided transparent cuvettes with a 10 mm path length, including borosilicate glass cuvettes and plastic cuvettes (1702415, Bio-Rad, Hercules, CA, USA)[24]. Reference spectra for spectral unmixing were first measured from corresponding single-stained samples under the same laser power and exposure settings used for multiplex imaging. For each fluorophore, a fluorescence-positive region was selected, and the mean fluorescence spectrum was exported as a reference profile. CMOS-mode acquisition was performed first using the CMOS acquisition workflow (**Supplementary**

Fig. 12b). CD31–DyLight® 755, TAG-1–FITC, and POPO®-1 were sequentially acquired using 730 nm excitation (50 mW; 750 nm long-pass filter; 300 ms exposure), 488 nm excitation (20 mW; 520/40 nm band-pass filter; 300 ms exposure), and 405 nm excitation (20 mW; 425 nm long-pass filter; 300 ms exposure), respectively. Images were acquired in step-and-acquire mode at 20 µm z-steps over approximately 300 sections, corresponding to a total travel distance of 6 mm. Hyperspectral imaging was then performed using the hyperspectral acquisition workflow (**Supplementary Fig. 12a**) with 647 and 561 nm excitation. RUNX2–Alexa Fluor® 647 and α-SMA–Cy5.5 were acquired under 647 nm excitation (50 mW, 675 nm long-pass filter; 300 ms exposure), and TNNI3–Cy3 and TUBB3–Alexa Fluor® 594 were acquired under 561 nm excitation (50 mW, 575 nm long-pass filter; 300 ms exposure). The total acquisition time was approximately 1.5 h for CMOS-mode imaging and approximately 47 h for hyperspectral imaging. The overall descSPIM-Galaxy imaging and processing workflow, including the selection of hyperspectral or CMOS detection and subsequent data integration, is summarized in **Supplementary Fig. 13**.

For SLIM imaging, two illumination configurations were used. In the three-color laser-diode-based configuration, E12.5 mouse embryos were stained in a total volume of 100 µL with POPO®-1 (20 µM) and two directly labeled primary antibodies, each at a final concentration of approximately 20 µg/mL: α-SMA labeled with Alexa Fluor® 647 using a Lightning-Link® Conjugation Kit (Fast) (ab269823, Abcam) and CD31 labeled with Alexa Fluor® 568 using a Lightning-Link® Conjugation Kit (Fast) (ab269821, Abcam). Samples were excited at 405, 520, and 639 nm, and emission was detected using band-pass filters with center wavelengths/full widths at half maximum of 450/40 nm (FBH450-40, Thorlabs), 600/40 nm (FBH600-40, Thorlabs), and 692/40 nm (#67-038, Edmund Optics), respectively. In the four-color fiber-coupled laser configuration, E12.5 mouse embryos were stained in a total volume of 100 µL with POPO®-1 (20 µM) and α-SMA–FITC, TUBB3–Alexa Fluor® 594,

and RUNX2–Alexa Fluor® 647, each at a final concentration of approximately 20 µg/mL. Samples were excited at 405, 488, 561, and 640 nm, respectively. Emission was detected using band-pass filters with center wavelengths/full widths at half maximum of 450/40 nm, 550/40 nm (FBH550-40, Thorlabs), 620/60 nm (#33-910, Edmund Optics), and 692/40 nm, respectively. Samples were embedded in CUBIC-R+ agarose inside five-sided transparent synthetic quartz cuvettes (10 × 10 × 45 mm; 0247151205, Tokyo Garasu Kikai). The exposure time was set to 800 ms, and the imaging range was 12 mm. Multicolor imaging was performed by sequential acquisition of independent 3D stacks for each channel.

Embryonic kidney

Embryonic kidneys were dissected from P17 embryos, fixed overnight in 4% PFA, washed in PBS and incubated overnight at 37°C in in 500 µL CUBIC-L. Prior to staining, samples were pre-incubated for 30 min in staining buffer (see above). Staining was performed overnight at 4 °C in staining buffer supplemented with Alexa Fluor® 555 NHS Ester (1:100, Thermo Fisher Scientific) and propidium iodide (1:500, Invitrogen), followed by washing (1 × 30 min in staining buffer and 2 × 30 min in PBS). Cleared samples were subsequently processed 2 × 3 hours CUBIC-X1 at RT and 2 × 3 hours in CUBIC-X2 at RT[31]. Cleared samples were transferred to a 5 mm path length quartz cuvette (UQ-203, Portmann Instruments) for imaging. Optical sections were recorded at 1.56 µm z-intervals across a 780 µm axial range (500 planes), with each plane exposed for 200 ms. Fluorescence was excited sequentially at 488 and 561 nm and collected through 525/50 (Chroma) and 600/70 (Chroma) emission bandpass filters, respectively.

Adult mouse lung

Adult mouse lung was dissected from transgenic B6N.Cg-Tg(Sftpc,-EGFP)1Dobb/J mice, fixed overnight in 4% PFA, and washed in PBS. A 3 mm tissue piece was prepared using a

biopsy punch and incubated overnight at 37°C in 500 µL CUBIC-L. A staining buffer containing 30% tetrahydrofuran (≥99.9%, anhydrous, inhibitor-free, Sigma-Aldrich), 0.5 M NaCl (Sigma-Aldrich), in 0.05 M acetate buffer at pH 5 was prepared. Prior to staining, samples were pre-incubated in staining buffer for 30 min. Staining was performed overnight at 4 °C in staining buffer supplemented with Atto594 NHS Ester (1:100, ATTO-TEC, Siegen, Germany) and propidium iodide (1:500, Invitrogen), followed by washing (1 × 30 min in staining buffer and 2 × 30 min in PBS). To enhance GFP signal, samples were incubated overnight at 35°C in HEPES-TSC buffer (10 mM HEPES (pH 7.5), containing 0.1% (v/v) Triton X-100 and 200 mM NaCl) supplemented with FluoTag®-X4 anti-GFP (1:200, NanoTag Biotechnologies, Göttingen, Germany), followed by washing (3 × 30 min in labeling buffer). Cleared samples were subsequently processed 2 × 3 hours CUBIC-X1 at RT and 2 × 3 hours in CUBIC-X2 at RT[31]. Cleared samples were transferred to a 5 mm path length quartz cuvette (UQ-203, Portmann Instruments) for imaging. The cuvette was mounted in the sample holder. Volumes were acquired using sequential excitation at 488, 532, 591 nm with an exposure time of 200 ms per plane. Optical sections were collected at a z-step of 1.94 µm over an axial range of 970 µm (500 planes). The piezo-driven filter slider contained one emission filter per laser, 525/50 (Chroma) for the 491 nm excitation, 600/70 (Chroma) for the 561 nm excitation and 705/72 (Chroma) for the 591 nm excitation.

Expanded mouse whole brain

ICR mice (Crl:CD1, Charles River) were purchased from KBT Oriental (Saga, Japan). Mice were deeply anesthetized with sodium pentobarbital (100 mg/kg, i.p.). After transcardial perfusion with PBS containing heparin followed by 4% PFA in PBS, the brain was collected and immersion-fixed in 4% PFA in PBS at 4 °C overnight. After PBS wash, samples were

822 immersed in CUBIC-1 (FUJIFILM CUBIC TRIAL KIT, FUJIFILM Wako Pure Chemical
823 Corporation, Osaka, Japan) or 25% urea supplemented CUBIC-L (CUBIC stars) and incubated
824 for 4–7 days at 37 °C with gentle shaking[31,49,50]. Staining was performed using CUBIC-HV2.0
825 (CUBIC stars) for 1–2 weeks[48]. SYTOX® Green (8 nmol, S7020, Thermo Fisher Scientific),
826 an anti-tyrosine hydroxylase antibody (1 µg, ab137869, Abcam), an anti-tryptophan
827 hydroxylase 2 antibody (1 µg, AMAb91108, Merck, Darmstadt, Germany), Alexa Fluor® 647
828 Fab Fragment Anti-Rabbit IgG (4.25 µg, 111-607-008, Jackson ImmunoResearch
829 Laboratories), and Cy3 Fab Fragment Anti-Mouse IgG1 (4.25 µg, 115-167-185, Jackson
830 ImmunoResearch Laboratories) were used for nuclear staining and immunostaining,
831 respectively, with CUBIC-HV2.0 additives A and B in 100 µL staining buffer[48]. Samples were
832 then immersed in CUBIC-X1 (Tokyo Chemical Industry) at 4 °C for 2 days and in CUBIC-X2
833 (Tokyo Chemical Industry) at room temperature for 2 days and embedded in 2% agarose
834 dissolved in CUBIC-X2 inside a 20 mm four-sided transparent cuvette[31].

835 Samples were scanned with Fullmoon using NIS-Element (Nikon, Tokyo, Japan).
836 Cleared samples mounted in cuvettes were imaged during continuous sample translation
837 through the light sheet while compensating focus with the detection stage. Samples were
838 excited with 488, 561, and 647 nm lasers, and emission was detected using a 50-nm band-pass
839 filter centered at 525 nm, and long-pass filters at 575 and 675 nm, respectively. Laser power
840 was typically 2–20 mW, with 250–500 ms exposure time.

841 **Rat brain slice**

842 Sprague–Dawley rats (Crl:CD, Charles River) were purchased from KBT Oriental. Rats
843 were deeply anesthetized with sodium pentobarbital (100 mg/kg, i.p.). After transcardial
844 perfusion with PBS containing heparin followed by 4% PFA in PBS, the brain was collected
845 and immersion-fixed in 4% PFA in PBS at 4 °C overnight. After PBS wash, samples were cut

into 2-mm-thick coronal sections and incubated in CUBIC-L (CUBIC stars) for 7 days at 37 °C with gentle shaking. Staining was performed using CUBIC-HV2.0 (CUBIC stars) for 1 week[48]. SYTOX® Green (8 nmol) was used for nuclear staining with CUBIC-HV2.0 additives A and B in 100 μL staining buffer. Samples were then immersed in 50% CUBIC-R+ (CUBIC stars) for 1 day and CUBIC-R+ for 2 days at 25 °C with gentle shaking. Samples were embedded in 2% agarose dissolved in CUBIC-R+ inside a 20 mm four-sided transparent cuvette[50].

Samples were captured with Fullmoon using NIS-Element (Nikon, Tokyo, Japan). Samples were excited with a 488 nm laser, and emission was detected using a 50-nm band-pass filter centered at 525 nm.

Image processing and reconstruction

For Galaxy, separate workflows were used for the 11-color fluorescent bead optical phantom and the 7-color whole-embryo dataset. Raw images of Galaxy were 470–900 nm spectral images with a spectral sampling interval of approximately 2.1 nm and monochrome CMOS images.

For the 11-color fluorescent bead optical phantom, reference spectra were constructed from single-color bead spectra after excluding spectral channels below the long-pass cutoff for each excitation condition (**Supplementary Fig. 6**). For 488 nm excitation, the reference spectral matrices included Alexa Fluor® 488, 514, 568 and 594. For 561 nm excitation, Alexa Fluor® 568, 594, 633 and 647 were used. For 647 nm excitation, Alexa Fluor® 633, 647, 660 and 700 were used. For 730 nm excitation, Alexa Fluor® 750 and 790 were used. Spectral unmixing was then performed using non-negative least-squares unmixing (NNLS)[51]. NNLS was applied with non-negativity constraints to estimate fluorophore contributions in the 488 nm-, 561 nm-, 647 nm- and 730 nm-excited datasets, generating unmixed image stacks for each

excitation condition. For the 405 nm-excited dataset, Alexa Fluor® 405 was processed separately by averaging the three shortest-wavelength bands (471.7–480.8 nm) for each z-slice, followed by background estimation using a circular ROI with a radius of 15 pixels to suppress local bright structures, threshold-based masking at $\mu + 3\sigma$, where μ was the mean pixel intensity and σ was fixed at 3.0, removal of objects smaller than 10 pixels to reduce isolated noise, and intensity normalization. For Alexa Fluor® 700, the unmixed stack was further processed by subtracting, on a slice-by-slice basis, the mean raw spectral signal from 671.8–674.0 nm, followed by lower clipping to the measured background value and final conversion to 8-bit data. For visualization, all image rendering and projection steps were performed in Fiji/ImageJ[46].

For the Galaxy 7-color whole-embryo dataset, hyperspectral datasets were preprocessed by interpolating reference spectra and extracting valid spectral bands above the long-pass cutoff for each excitation condition (**Supplementary Fig. 6**). Separate reference spectral matrices were constructed for the 647 nm- and 561 nm-excited datasets using representative spectral bands containing signals. Linear spectral unmixing was then performed slice-by-slice along the *z*-stack using NNLS to separate RUNX2–Alexa Fluor® 647 and α-SMA–Cy5.5 from the 647 nm-excited data, and TNNI3–Cy3 and TUBB3–Alexa Fluor® 594 from the 561 nm-excited data[52]. The unmixed planes were concatenated into multipage TIFF stacks representing the three-dimensional distribution of each fluorophore, whereas 405 excitated image data were averaged across selected bands before stack generation.

Because POPO®-1 was acquired using both CMOS and hyperspectral detection in the Galaxy 7-color embryo experiment, and because the FOV and pixel size differed between the two cameras, the CMOS TIFF stacks (2160 × 4096 pixels, 3.45 × 3.45 μm per pixel) were resampled to match the 5.5 × 5.5 μm per pixel hyperspectral dataset and transformed onto the

fixed 1088 × 2048-pixel hyperspectral image canvas for cross-camera registration (**Supplementary Fig. 7**). After pixel-size matching, the CMOS stacks were aligned to the hyperspectral reference using the Enhanced Correlation Coefficient (ECC) image-alignment algorithm for Euclidean and affine registration, followed by SyN-based nonlinear registration with ANTs[24,53,54,55]. Registration performance was evaluated by normalized cross-correlation (NCC) mapping using the POPO®-1 nuclear signal as a common reference channel, and the SyN parameter set yielding the highest correlation was adopted for subsequent analyses (**Supplementary Fig. 4**). When residual in-plane misalignment remained after nonlinear registration, a manual post-registration *x*–*y* shift correction was applied as necessary, and its effect was evaluated by marker-pair correlation analysis (**Supplementary Fig. 5**). The resulting transformation parameters were then applied to the CMOS-derived TAG-1 and CD31 channels to align them with the hyperspectral dataset. Final registered multicolor image stacks were converted to 8-bit TIFF and merged in Fiji/ImageJ. Maximum-intensity projections were generated in Fiji/ImageJ, and three-dimensional renderings were generated in Imaris (version 11.0.1; Oxford Instruments)[46]. The overall Galaxy 7-color imaging and image-processing workflow, including spectral preprocessing, linear unmixing, cross-camera registration and post-registration correction, is summarized in **Supplementary Figs. 4 and 5**, with the corresponding analysis scripts provided on GitHub.

For Deepsky, we calculated the FWHM of the beads by applying 3D connected component analysis to the image stack and fitting a 1D smoothed spline for each dimension (UnvariateSpline, scipy). The tiled datasets were aligned using BigStitcher and rendered in Imaris v10.2[56] . False-color H&E-like images were generated computationally using FalseColor-Python[29]. GFP positive cells were counted using Spot Detection in Imaris 11.0.1 (Oxford Instruments) with “spot diameter: 10.0 μm”, “background subtraction: True” and “Quality > 26.89”. To estimate the total tissue volume, a surface was created on the nuclei

channel with the “Enable Smooth = true”, “Surface Grain Size = 50.00 μm” and “Manual Threshold Value = 59.9812”.

For Fullmoon and SLIM, images were processed in Fiji/ImageJ and rendered in three dimensions using Fiji/ImageJ and Aivia Community[46]. Pixel size and z-step interval were assigned in Image Properties, and representative images were generated by maximum-intensity projection. Tph2-positive cells were counted using ilastik and ImageJ[46,57]. The images were cropped to include all Tph2-positive cells, and the positive cells were segmented using ilastik. The number of cells was then counted using ImageJ with the 3D ImageJ Suite plugin[58]. The detection accuracy was 97.0% in sparsely distributed regions and 89.2% in densely clustered regions. For SLIM datasets, split TIFF stacks were concatenated into full stacks, and when stripe artifacts were observed, a 3 × 3 median filter was applied before color assignment and projection.

Data availability

The imaging data obtained in this study are available from the corresponding author upon reasonable request. Raw volumetric imaging datasets, including hyperspectral image stacks, large-field volumetric datasets and expanded-sample image data, are too large to be provided with this paper. Requests for data access will be reviewed and fulfilled within a reasonable timeframe, subject to data size, transfer feasibility and institutional data-sharing policies. Source data underlying the quantitative graphs and summary measurements are provided with this paper.

Code availability

Custom code and documentation generated for descSPIM-Advanced are available at https://github.com/dbsb-juntendo/descSPIM-Advanced. The repository includes the Mission Control Center control software, installation instructions, device-control modules, imaging workflows, image-processing pipelines and construction-related resources for the descSPIM-Advanced configurations. Additional implementation details are available from the corresponding author upon reasonable request.

References

1. Susaki, E. A. & Ueda, H. R. Whole-body and Whole-Organ Clearing and Imaging Techniques with Single-Cell Resolution: Toward Organism-Level Systems Biology in Mammals. *Cell Chem. Biol.* **23**, 137–157 (2016).

2. Ueda, H. R. *et al.* Whole-brain profiling of cells and circuits in mammals by tissue clearing and light-sheet microscopy. *Neuron* **106**, 369–387 (2020).

3. Mitani, T. T., Susaki, E. A., Matsumoto, K. & Ueda, H. R. Realization of cellomics to dive into the whole-body or whole-organ cell cloud. *Nat. Methods* **21**, 1138–1142 (2024).

4. Ueda, H. R. *et al.* Tissue clearing and its applications in neuroscience. *Nat. Rev. Neurosci.* **21**, 61–79 (2020).

5. Richardson, D. S. *et al.* Tissue clearing. *Nat. Rev. Methods Primer* **1**, 84 (2021).

6. Voie, A. H., Burns, D. H. & Spelman, F. A. Orthogonal-plane fluorescence optical sectioning: Three-dimensional imaging of macroscopic biological specimens. *J. Microsc.* **170**, 229–236 (1993).

7. Dodt, H.-U. *et al.* Ultramicroscopy: three-dimensional visualization of neuronal networks in the whole mouse brain. *Nat. Methods* **4**, 331–336 (2007).

8. Ueda, H. R. *et al.* Tissue clearing and its applications in neuroscience. *Nat. Rev. Neurosci.* **21**, 61–79 (2020).

9. Huisken, J., Swoger, J., Del Bene, F., Wittbrodt, J. & Stelzer, E. H. K. Optical Sectioning Deep Inside Live Embryos by Selective Plane Illumination Microscopy. *Science* **305**, 1007–1009 (2004).

10. Keller, P. J., Schmidt, A. D., Wittbrodt, J. & Stelzer, E. H. K. Reconstruction of Zebrafish Early Embryonic Development by Scanned Light Sheet Microscopy. *Science* **322**, 1065–1069 (2008).

11. Huisken, J. & Stainier, D. Y. R. Even fluorescence excitation by multidirectional selective plane illumination microscopy (mSPIM). *Opt. Lett.* **32**, 2608–2610 (2007).

12. Wang, D., Jin, Y., Feng, R., Chen, Y. & Gao, L. Tiling light sheet selective plane illumination microscopy using discontinuous light sheets. *Opt. Express* **27**, 34472–34483 (2019).

13. Chen, Y. *et al.* A versatile tiling light sheet microscope for imaging of cleared tissues. *Cell Rep.* **33**, (2020).

14. Dean, K. M., Roudot, P., Welf, E. S., Danuser, G. & Fiolka, R. Deconvolution-free subcellular imaging with axially swept light sheet microscopy. *Biophys. J.* **108**, 2807–2815 (2015).

15. Medeiros, G. de *et al.* Confocal multiview light-sheet microscopy. *Nat. Commun.* **6**, 8881 (2015).

16. Baumgart, E. & Kubitscheck, U. Scanned light sheet microscopy with confocal slit detection. *Opt. Express* **20**, 21805–21814 (2012).

17. Pitrone, P. G. *et al.* OpenSPIM: an open-access light-sheet microscopy platform. *Nat. Methods* **10**, 598–599 (2013).

18. Gualda, E. J. *et al.* OpenSpinMicroscopy: an open-source integrated microscopy platform. *Nat. Methods* **10**, 599–600 (2013).

19. Voigt, F. F. *et al.* The mesoSPIM initiative: open-source light-sheet microscopes for imaging cleared tissue. *Nat. Methods* **16**, 1105–1108 (2019).

20. Vladimirov, N. *et al.* Benchtop mesoSPIM: a next-generation open-source light-sheet microscope for cleared samples. *Nat. Commun.* **15**, 2679 (2024).

21. Hedde, P. N. miniSPIM-A Miniaturized Light-Sheet Microscope. *ACS Sens.* **6**, 2654–2663 (2021).

994 22. Diederich, B. *et al.* A versatile and customizable low-cost 3D-printed open standard for
995 microscopic imaging. *Nat. Commun.* **11**, 5979 (2020).
996 23. Chen, Y. *et al.* Low-cost and scalable projected light-sheet microscopy for the high-
997 resolution imaging of cleared tissue and living samples. *Nat. Biomed. Eng.* **8**, 1109–1123
998 (2024).
999 24. Otomo, K. *et al.* descSPIM: an affordable and easy-to-build light-sheet microscope
1000 optimized for tissue clearing techniques. *Nat. Commun.* **15**, 4941 (2024).
1001 25. Gong, C. *et al.* Hybrid solid−liquid optics enable scalable, high-resolution light-sheet
1002 microscopy across diverse immersion media. *Nat. Biotechnol.* 1–13 (2026)
1003 doi:10.1038/s41587-026-03172-7.
1004 26. Aakhte, M. *et al.* Isotropic, aberration-corrected light sheet microscopy for rapid high-
1005 resolution imaging of cleared tissue. *Nat. Biotechnol.* 1–11 (2025).
1006 27. Susaki, E. A. Unlocking the potential of large-scale 3D imaging with tissue clearing
1007 techniques. *Microscopy* **74**, 179–188 (2025).
1008 28. Pichette, J., Charle, W. & Lambrechts, A. Fast and compact internal scanning CMOS-
1009 based hyperspectral camera: the Snapscan. in *Photonic Instrumentation Engineering IV* vol.
1010 10110 292 (SPIE, 2017).
1011 29. Serafin, R., Xie, W., Glaser, A. K. & Liu, J. T. C. FalseColor-Python: A rapid intensity-
1012 leveling and digital-staining package for fluorescence-based slide-free digital pathology.
1013 *PLoS ONE* **15**, e0233198 (2020).
1014 30. Vanderbilt, J. N. *et al.* High-Efficiency Type II Cell–Enhanced Green Fluorescent
1015 Protein Expression Facilitates Cellular Identification, Tracking, and Isolation. *Am. J.*
1016 *Respir. Cell Mol. Biol.* **53**, 14–21 (2015).

31. Murakami, T. C. *et al.* A three-dimensional single-cell-resolution whole-brain atlas using CUBIC-X expansion microscopy and tissue clearing. *Nat. Neurosci.* **21**, 625–637 (2018).

32. Jahr, W., Schmid, B., Schmied, C., Fahrbach, F. O. & Huisken, J. Hyperspectral light sheet microscopy. *Nat. Commun.* **6**, 1–7 (2015).

33. Crombez, S., Leclerc, P., Ray, C. & Ducros, N. Computational hyperspectral light-sheet microscopy. *Opt. Express* **30**, 4856–4866 (2022).

34. Crombez, S., Ray, C., Exbrayat-Héritier, C., Ruggiero, F. & Ducros, N. Hyperspectral LSFM with DMD-only shaping and neural network reconstruction. *Opt. Express* **33**, 52339–52355 (2025).

35. Morizet, J. *et al.* UVA Hyperspectral Light-Sheet Microscopy for Volumetric Metabolic Imaging: Application to Preimplantation Embryo Development. *ACS Photonics* **10**, 4177–4187 (2023).

36. Wang, P. *et al.* A single-shot hyperspectral phasor camera for fast, multi-color fluorescence microscopy. *Cell Rep. Methods* **3**, (2023).

37. Lavagnino, Z. *et al.* Snapshot hyperspectral light-sheet imaging of signal transduction in live pancreatic islets. *Biophys. J.* **111**, 409–417 (2016).

38. Lin, J.-R. *et al.* Highly multiplexed immunofluorescence imaging of human tissues and tumors using t-CyCIF and conventional optical microscopes. *eLife* **7**, e31657 (2018).

39. Gut, G., Herrmann, M. D. & Pelkmans, L. Multiplexed protein maps link subcellular organization to cellular states. *Science* **361**, eaar7042 (2018).

40. Goltsev, Y. *et al.* Deep Profiling of Mouse Splenic Architecture with CODEX Multiplexed Imaging. *Cell* **174**, 968-981.e15 (2018).

41. Yau, C. N. *et al.* INSIHGT: an accessible multi-scale, multi-modal 3D spatial biology platform. *Nat. Commun.* **15**, 10888 (2024).

42. Lin, Y.-H. *et al.* Revealing intact neuronal circuitry in centimeter-sized formalin-fixed paraffin-embedded brain. *eLife* **13**, RP93212 (2024).

43. Edelstein, A., Amodaj, N., Hoover, K., Vale, R. & Stuurman, N. Computer Control of Microscopes Using μManager. *Curr. Protoc. Mol. Biol.* **92**, (2010).

44. Edelstein, A. D. *et al.* Advanced methods of microscope control using μManager software. *J. Biol. Methods* **1**, e10 (2014).

45. Moreno, X. C., Al-Kadhimi, S., Alvelid, J., Bodén, A. & Testa, I. ImSwitch: Generalizing microscope control in Python. *J. Open Source Softw.* **6**, 3394 (2021).

46. Schindelin, J. *et al.* Fiji: an open-source platform for biological-image analysis. *Nat. Methods* **9**, 676–682 (2012).

47. Matsumoto, K. *et al.* Advanced CUBIC tissue clearing for whole-organ cell profiling. *Nat. Protoc.* **14**, 3506–3537 (2019).

48. Susaki, E. A., Kurusu, R. & Saito, Y. CUBIC-HistoVIsion2.0, published on Feb 25, 2026. https://www.protocols.io/view/cubic-histovision2-0-n92ld1wyxl5b/v1 (2026).

49. Susaki, E. A. *et al.* Whole-brain imaging with single-cell resolution using chemical cocktails and computational analysis. *Cell* **157**, 726–739 (2014).

50. Tainaka, K. *et al.* Chemical landscape for tissue clearing based on hydrophilic reagents. *Cell Rep.* **24**, 2196–2210 (2018).

51. Lawson, C.L. and Hanson, R.J. (1974) Solving Least Squares Problems. Prentice-Hall, Englewood Cliffs. - References - Scientific Research Publishing. https://www.scirp.org/reference/referencespapers?referenceid=2549470.

52. Ling, R. F., Lawson, C. L. & Hanson, R. J. Solving Least Squares Problems. in *Journal of the American Statistical Association* vol. 72 930 (1977).

53. Mano, T. *et al.* CUBIC-Cloud provides an integrative computational framework toward community-driven whole-mouse-brain mapping. *Cell Rep. Methods* **1**, 100038 (2021).

54. Avants, B. B., Epstein, C. L., Grossman, M. & Gee, J. C. Symmetric diffeomorphic image registration with cross-correlation: evaluating automated labeling of elderly and neurodegenerative brain. *Med. Image Anal.* **12**, 26–41 (2008).

55. Evangelidis, G. D. & Psarakis, E. Z. Parametric Image Alignment Using Enhanced Correlation Coefficient Maximization. *IEEE Trans. Pattern Anal. Mach. Intell.* **30**, 1858–1865 (2008).

56. Hörl, D. *et al.* BigStitcher: reconstructing high-resolution image datasets of cleared and expanded samples. *Nat. Methods* **16**, 870–874 (2019).

57. Berg, S. *et al.* ilastik: interactive machine learning for (bio)image analysis. *Nat. Methods* **16**, 1226–1232 (2019).

58. Ollion, J., Cochennec, J., Loll, F., Escudé, C. & Boudier, T. TANGO: a generic tool for high-throughput 3D image analysis for studying nuclear organization. *Bioinformatics* **29**, 1840–1841 (2013).

Acknowledgements

We thank Y. Ohinata (Chiba University, Japan) and H. Higashiyama (SOKENDAI, Japan) for valuable discussions and suggestions regarding embryonic marker proteins. We also thank A. Kanemitsu, K. Suzuki, Y. Kumagai, S. Ryu, and R. Kurusu (Department of Biochemistry and Systems Biomedicine, Juntendo University Graduate School of Medicine) for their helpful advice and support, including the fluorescent beads preparation and animal experiments; T. Yao (Juntendo University Faculty of Medicine, Japan) for assistance with preparing the 3D CAD models of descSPIM-SLIM; Laboratory of Molecular and Biochemical Research, Biomedical Research Core Facilities, and Laboratory II, Center for Biomedical Research Resources, Juntendo University, for animal experiments; Alexandros Sountoulidis and Christos Samakovlis for providing the mouse lung sample, and Giovanna Coceano and Ilaria

Testa for providing the embryonic rat kidney sample. We also acknowledge the ALM facility at KTH and the National Microscopy Infrastructure, NMI (VR-RFI 2019-00217). We also appreciate CUBICStars Inc., Oxford Instruments and Kantum Ushikata Co., LTD. for their technical supports. We used ChatGPT (OpenAI), Gemini (Google), and Claude Code (Anthropic) to assist with coding tasks and to refine the wording of the manuscript. The authors take full responsibility for the content of the manuscript.

Fundings

This work was supported by AMED Brain/MINDS 2.0 (JP25wm0625105 to K.O.); AMED Project for Promotion of Cancer Research and Therapeutic Evolution (P-PROMOTE) (JP25ama221610 to E.A.S.); AMED SCARDA (JP223fa827004 to K.N.); JST CREST (JPMJCR20E4 to K.O. and JPMJCR23B7 to E.A.S.); JST FOREST (JPMJFR230R to K.O.); JSPS KAKENHI Grant-in-Aid for Scientific Research (B) (JP22H02756 and JP25K02402 to K.O.; JP23K23788, JP24K01925, and JP25K02179 to K.N.); JSPS KAKENHI Grant-in-Aid for Scientific Research (A) (JP25H01025 to K.O.; JP23H00360 to K.N.); JSPS KAKENHI Grant-in-Aid for Challenging Research (Exploratory) (JP23K18081 and JP26K23116 to K.N.); JSPS KAKENHI Grant-in-Aid for Transformative Research Areas, Platforms for Advanced Technologies and Research Resources “Advanced Bioimaging Support” (JP22H04926 to E.A.S.); JSPS KAKENHI International Leading Research (JP23K20044 to E.A.S.); Operating Costs Subsidies for Private Universities (to E.A.S.); Grants-in-Aid from UTEC-UTokyo (to E.A.S.); the Takeda Science Foundation (to E.A.S.); the Nakatani Foundation (to E.A.S.); a joint research program with Kantum Ushikata Co., LTD. (to E.A.S.); the Swedish Research Council (Vetenskapsrådet, VR 2020-05347, to H.B.); the Uehara Memorial Foundation (to K.N.), the Naito Foundation (to K.O.), and the Vehicle Racing Commemorative Foundation (#6580 to A. Kanemitsu, in collaboration with Y.N.).

Author contributions

E.A.S., K.O., H.B. and K.N. conceived and supervised the study. Y.N., S.E., K.N., M.S., K.O. and A.L.Y. designed, built and optimized the microscope systems and performed imaging experiments. Y.N., S.E., K.N., M.S. and K.O. generated the figure data. Y.Sato contributed to imaging experiments and assisted with instrument setup and optimization. Y.Saito assisted with sample preparation. K.N. developed the integrated control framework, and Y.N. and M.S. contributed to its debugging, refinement and implementation. T.N. and C.M. contributed to the establishment of the imaging workflow in part. Y.W. and Y.N. contributed to troubleshooting and debugging during imaging experiments. Y.N., S.E., K.N. and M.S. wrote the manuscript with input and revisions from E.A.S., K.O. and H.B. All authors contributed to discussion of the results and manuscript preparation.

Conflict of interest

E.A.S. receives long-term large-scale research funding from the Nakatani Foundation for FY2024–2028. E.A.S. is an executive officer and employee of CUBICStars Inc., a company that provides services based on CUBIC technology. E.A.S. is also named as a co-inventor on patents and patent applications owned by RIKEN and CUBICStars Inc., related to CUBIC reagents. The other authors declare no competing interests.

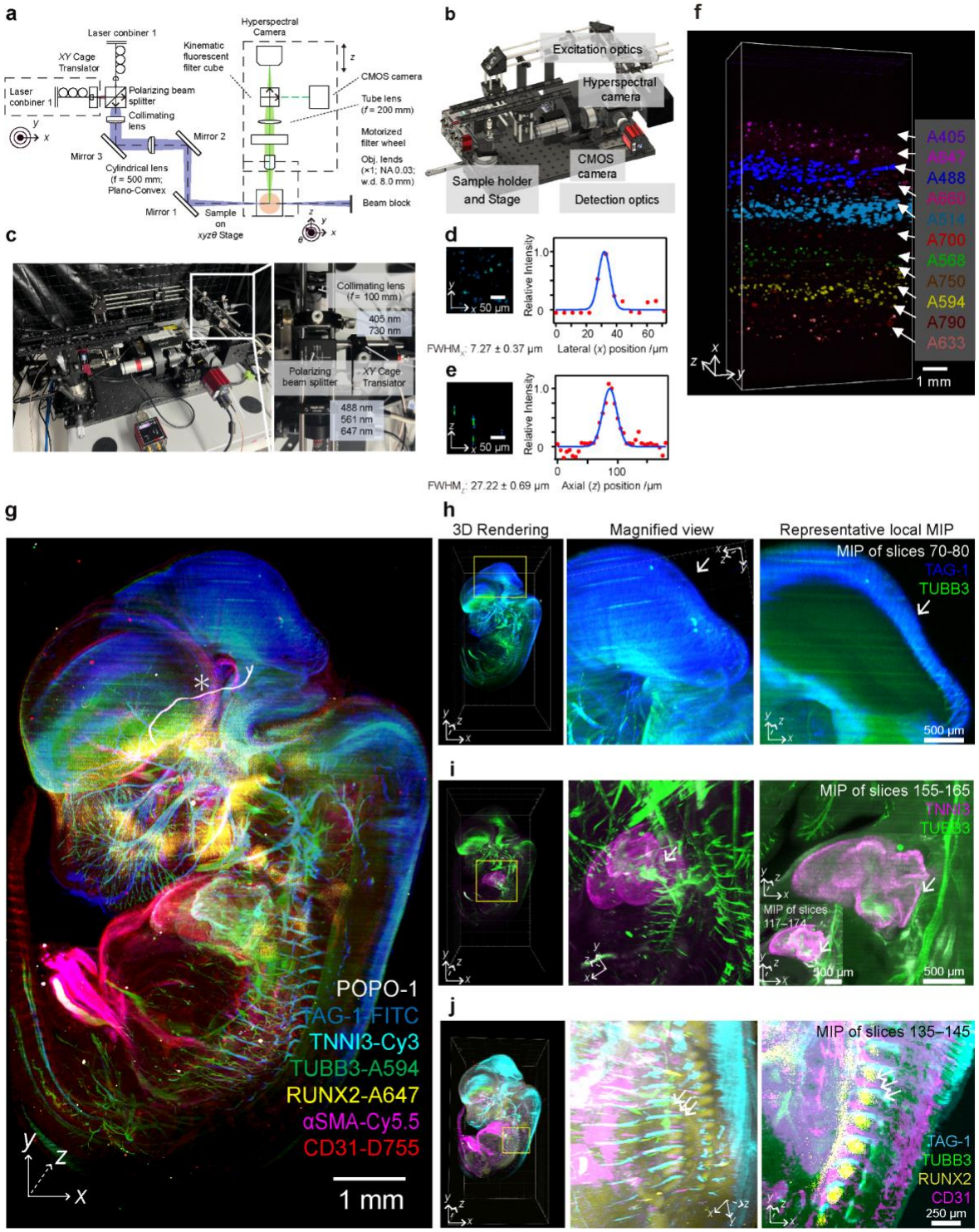


Fig. 1 | descSPIM-Galaxy enables multispectral 3D imaging at whole-embryo scale

a, Optical layout of descSPIM-Galaxy. Five excitation wavelengths are merged into a single illumination arm to generate a one-sided light sheet. Fluorescence is routed either to a CMOS camera or to a hyperspectral camera via a removable mirror and a motorized filter wheel, enabling sequential dual-path acquisition. **b,c,** Point spread function (PSF) measurements using

Φ1-µm fluorescent beads. Galaxy showed slightly lower lateral resolution than descSPIM-basic because of the larger pixel size of the hyperspectral camera (5.5 µm versus 3.45 µm in descSPIM-basic), whereas its axial resolution remained comparable to that of descSPIM-basic operated in full-FOV mode (26.0 µm). **d,e,** Instrument photograph and schematic. Cleared specimens are mounted in a four-sided transmission cuvette and imaged without an immersion chamber. **f,** multispectral imaging of an optical phantom composed of Protein A/G agarose beads, each labeled with a single Alexa Fluor® dye. Five excitation lines were used to acquire a 150-band hyperspectral dataset over a volume of 5.98 mm × 11.26 mm × 3.00 mm (x × y × z), and 11 spectrally overlapping fluorophores were separated by linear spectral unmixing. **g,** 7-color three-dimensional imaging of a cleared whole E12.5 mouse embryo. The full imaged volume was 5.98 mm × 11.26 mm × 6.00 mm (x × y × z), acquired in approximately 40 h in total, corresponding to approximately 7.5 h per channel, from which the embryo region was cropped for visualization. Selected channels were recorded on both detection paths and rigidly registered, whereas spectrally overlapping channels were acquired and unmixed using the hyperspectral detection path. The asterisk indicates an artifact located outside the embryonic body and derived from material distinct from embryonic tissue. **h–j,** Representative anatomical views from the 7-color whole-embryo dataset, shown as 3D renderings with corresponding 2D slice views. **h,** Comparison of the TAG1 and TUBB3 channels shows a more spatially restricted distribution of TAG1-positive signals in the dorsal telencephalic/cortical primordium relative to the broader TUBB3-positive neuronal signals, revealing region-dependent differences in neuronal signal distribution in the developing brain. **i,** TUBB3-positive neural structures are visualized around the TNNI3-positive embryonic heart, with trajectories compatible with those expected for the developing cardiac plexus. **j,** CD31-positive vascular structures and TUBB3/TAG1-positive intercostal nerves are visualized in close apposition between adjacent RUNX2-positive developing ribs. In multiple intercostal regions, the vascular structures are

positioned superior or rostral to the neural structures, consistent with the expected spatial organization of intercostal neurovascular bundles.

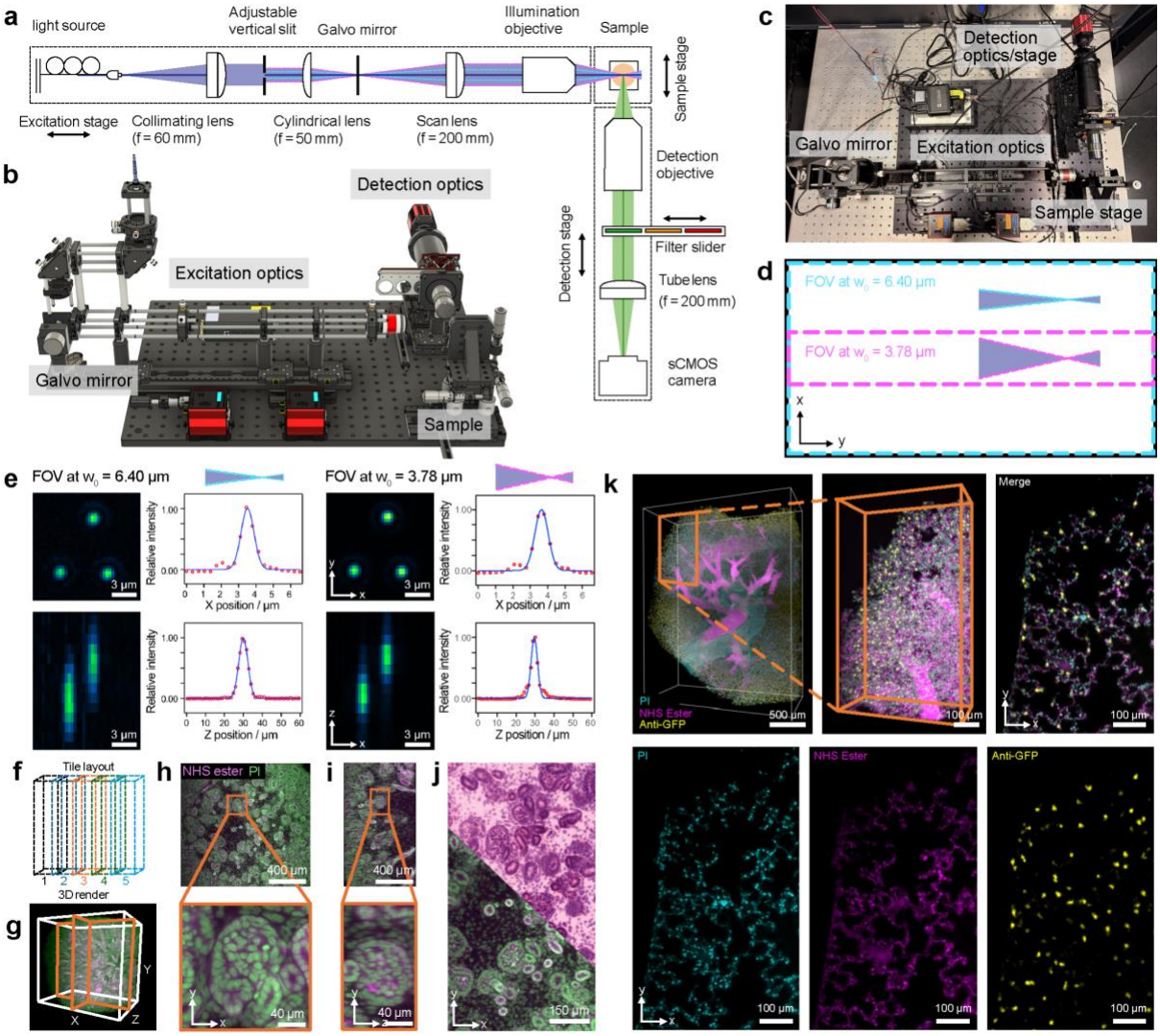


Fig. 2 | descSPIM-Deepsky enables high-resolution 3D histology with adjustable axial resolution

a, Schematic overview of descSPIM-Deepsky. On the excitation side, a light-sheet is created using a cylindrical lens. The effective light-sheet thickness can be modified using an adjustable vertical slit. The beam is scanned with a galvanometer mirror and projected onto the illumination objective with a scan lens. The fluorescent response of the sample is captured by the detection objective and focused onto the camera by a tube lens. A piezo-electric emission filter slider provides automated switching of emission filters. **b,** CAD rendering of descSPIM-Deepsky. **c,** Photograph of descSPIM-Deepsky. **d,** Usable FOV for thin (w0 = 3.78 µm) and thick (w0 = 6.40 µm) light-sheet. **e,** Axial and lateral resolution performance of descSPIM-

Deepsky in a calibration bead sample (200 nm diameter) with open and closed slit. **f,** Tile layout of a cleared rat embryonic kidney stained with Alexa 555 NHS ester labeling proteins (magenta) and propidium iodide labeling nuclei (green) with a thin light-sheet. **g,** 3D render after stitching. **h,** XY plane of the tiled image with zoomed-in ROI**. i,** YZ plane with zoomed-in ROI showing high axial resolution where individual nuclei can clearly be differentiated. **j,** Cropped ROI false-colored to resemble H&E staining. **k,** Tiled cleared mouse lung imaged with a closed slit (thick lightsheet). Nuclei were stained with propidium iodide (cyan), proteins were stained with Atto594 NHS Ester (magenta), and secretory cells were stained with anti-GFP nanobodies (yellow) showing 3D render, zoomed-in ROI and XY plane i. individual color channels. The representative Deepsky datasets were acquired in approximately 65 min for the kidney sample and 94 min for the lung sample.

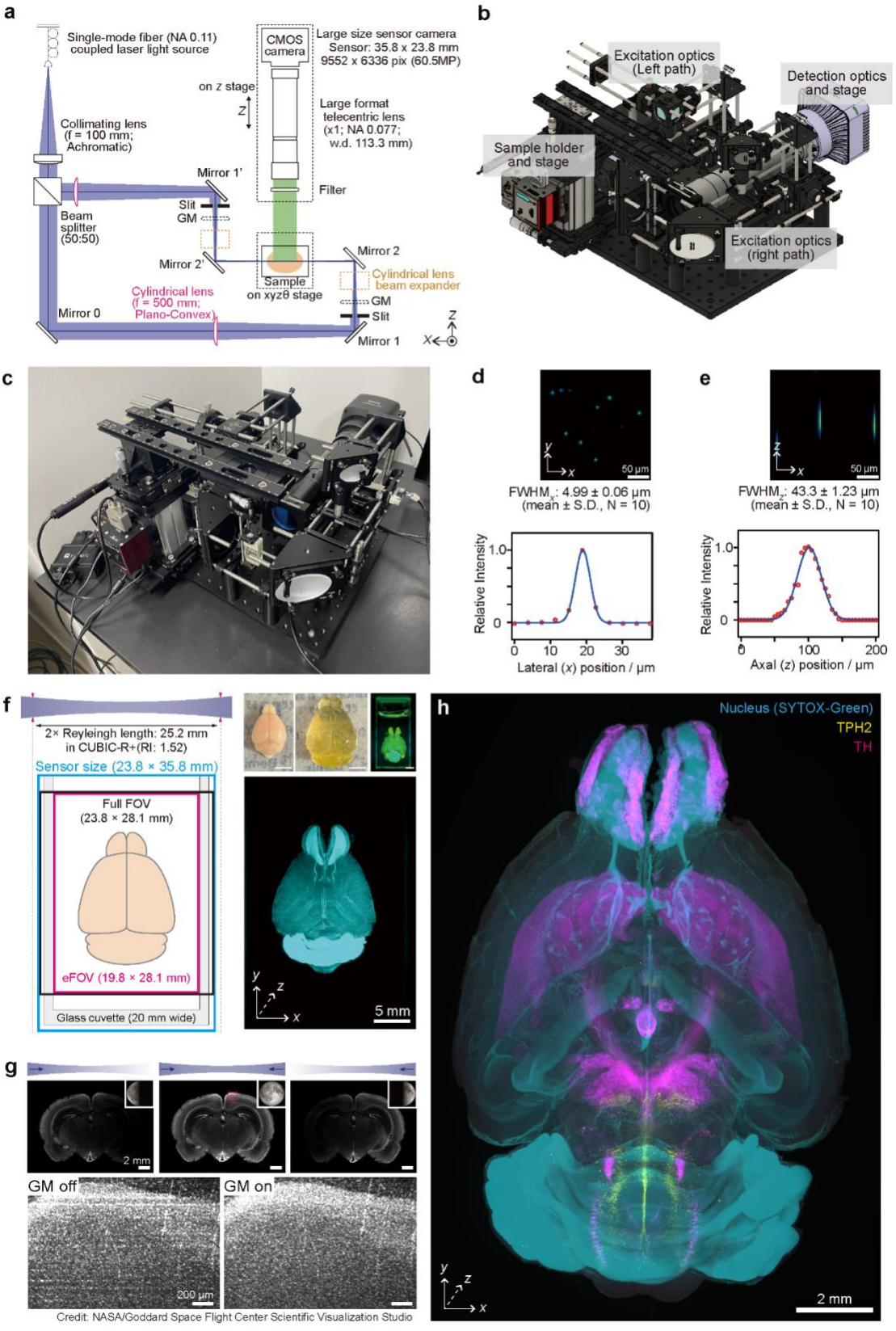


Fig. 3 | descSPIM-Fullmoon enables large field-of-view imaging of expanded whole brains in a single field of view

a, Optical layout of descSPIM-Fullmoon. Dual-sided light-sheet illumination generated using a collimating lens, a beam splitter, a cylindrical lens (f = 500 mm), and a slit, illuminated the sample from both sides. The galvanometer mirror (GM) and cylindrical lens beam expander enable pivoting of the light-sheet. The detection path is composed of a 1× large-format telecentric lens and a CMOS camera with a 23.8 mm × 35.8 mm sensor area, providing an effective magnification of 1× and a pixel size of 3.76 µm × 3.76 µm. **b,** 3D CAD model of the descSPIM-Fullmoon with the individual modules labeled. **c,** Actual view of the descSPIM-Fullmoon on a 30 × 45 mm breadboard. **d,e,** Measurement of lateral and axial resolutions based on PSF evaluated with Φ1 µm beads images. descSPIM-Fullmoon provides xy resolution (4.99 ± 0.06 µm, n = 10) comparable to descSPIM-basic (4.2 µm in FF mode). To achieve a wider FOV, its axial resolution was 43.3 ± 1.23 µm (n = 10), nearly twofold lower than that of descSPIM-basic operated in FF mode (26.0 µm). **f,** Relationship between the light-sheet, sensor size of camera, full FOV, eFOV and samples. The light-sheet covered the full width of the camera sensor (23.8 mm), although its height (28.1 mm) did not cover the full sensor height (35.8 mm). Because actual samples are imaged in a glass cuvette, the lateral extent of the FOV was limited by the width of the cuvette (20 mm, left panel). Therefore, the eFOV of the setup shown here was 19.8 mm × 28.1 mm, still enabling single-field imaging of a CUBIC-X-expanded whole mouse brain without tile stitching. The image on the right is a maximum intensity projection of an expanded whole mouse brain stained with SYTOX® Green. Upper panels show mouse brains before and after expansion, and mounted on the microscope in a 20-mm-wide cuvette. All scale bars are 5 mm. **g,** Effects of single- or dual-sided light-sheet illumination and light-sheet pivoting with a coronal section of a SYTOX® Green-stained rat brain. Dual-side illumination compensated for excitation light attenuation and achieved uniform illumination across FOV. Pivoting of the light-sheet by the galvanometer mirror (GM) effectively eliminated stripe shadow artifacts. **h,** 3D rendering of multicolor imaging of an

expanded whole mouse brain. descSPIM-Fullmoon also supports multicolor imaging using multi-track acquisition (acquisition time, 2.79 min per channel). Cyan: nucleus (SYTOX® Green); yellow: tryptophan hydroxylase 2 (Tph2, Cy3); magenta: tyrosine hydroxylase (Th, Alexa Fluor® 647).

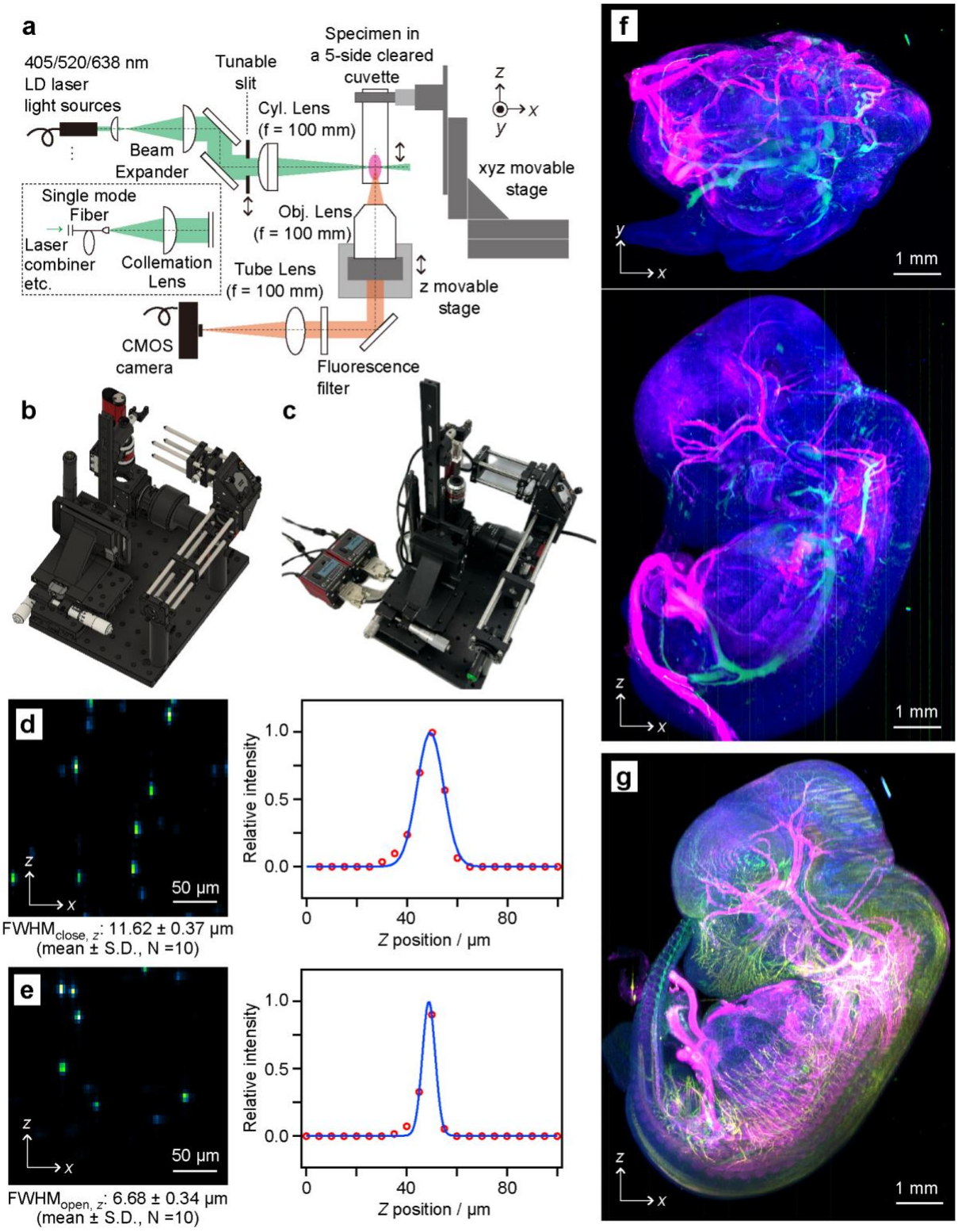


Fig. 4 | descSPIM-SLIM enables more affordable, easy-to-build, and rapidly deployable multicolor imaging

a, Overview of the descSPIM-SLIM system. A one-sided light-sheet is generated using a 10× beam expander and a cylindrical lens, with a tunable slit to adjust the effective excitation NA.

The detection path consists of a 2× objective lens, a tube lens, and a CMOS camera. **b,** Schematic overview of descSPIM-SLIM. **c,** Photograph of descSPIM-SLIM. **d,e,** Axial resolution estimation using Φ1 μm beads acquired with the tunable slit fully opened. GFB-pseudo colored bead images and the corresponding axial PSF plots are shown for 3 mm (d) and 6 mm (e) slit conditions. Lateral resolutions were comparable between slit widths (6 mm: 4.42 ± 0.23 μm; 3 mm: 4.43 ± 0.32 μm). **f,** Three-color volume rendering of a cleared E12.5 mouse embryo acquired with descSPIM-SLIM in approximately 20 min in total, corresponding to approximately 5 min per channel. Blue, POPO®-1; green, CD31–Alexa Fluor® 568; magenta, αSMA–Alexa Fluor® 647. **g,** Four-color imaging of a cleared E12.5 mouse embryo acquired with descSPIM-SLIM using a single-mode-fiber-coupled laser light source. Blue, POPO®-1; green, CD31–FITC; yellow, TUBB3–Alexa Fluor® 594; magenta, αSMA–Alexa Fluor® 647.

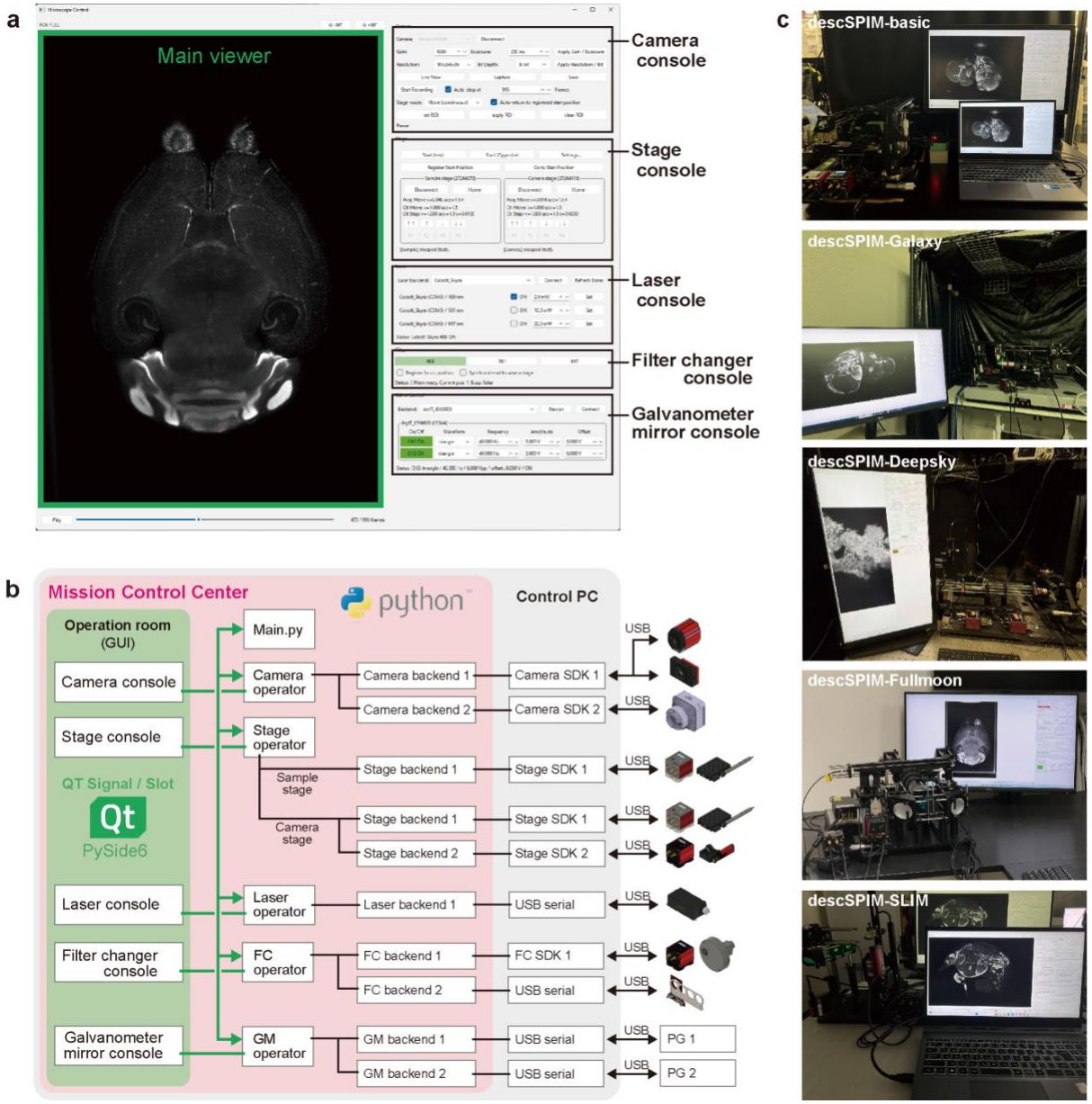


Fig. 5 | Mission Control Center for unified operation of the descSPIM-Advanced platform. **a,** Overview of graphical user interface (GUI) of MCC. The left region shows the main viewer for camera-acquired images. The right consoles enable connection and control of cameras, sample and camera stages, lasers, filter changers (FC), and pattern generators (PG) for driving galvanometer mirrors (GM). **b,** Architecture of MCC. Each console is associated with a corresponding operator, which controls the relevant devices through device-specific backend modules. Operators can interact with one another via main.py, enabling synchronized control across any combination of devices, such as camera–stage or filter changer–laser combinations.

This enabled automated multicolor imaging and multi-track acquisition. Device-specific control functions are implemented in independent backend modules, allowing additional hardware to be incorporated without modifying the main application code. **c,** Photographs showing operation of descSPIM variants using MCC: basic, Galaxy, Deepsky, Fullmoon, and SLIM. All descSPIM variants were successfully operated through MCC, and image data were acquired.

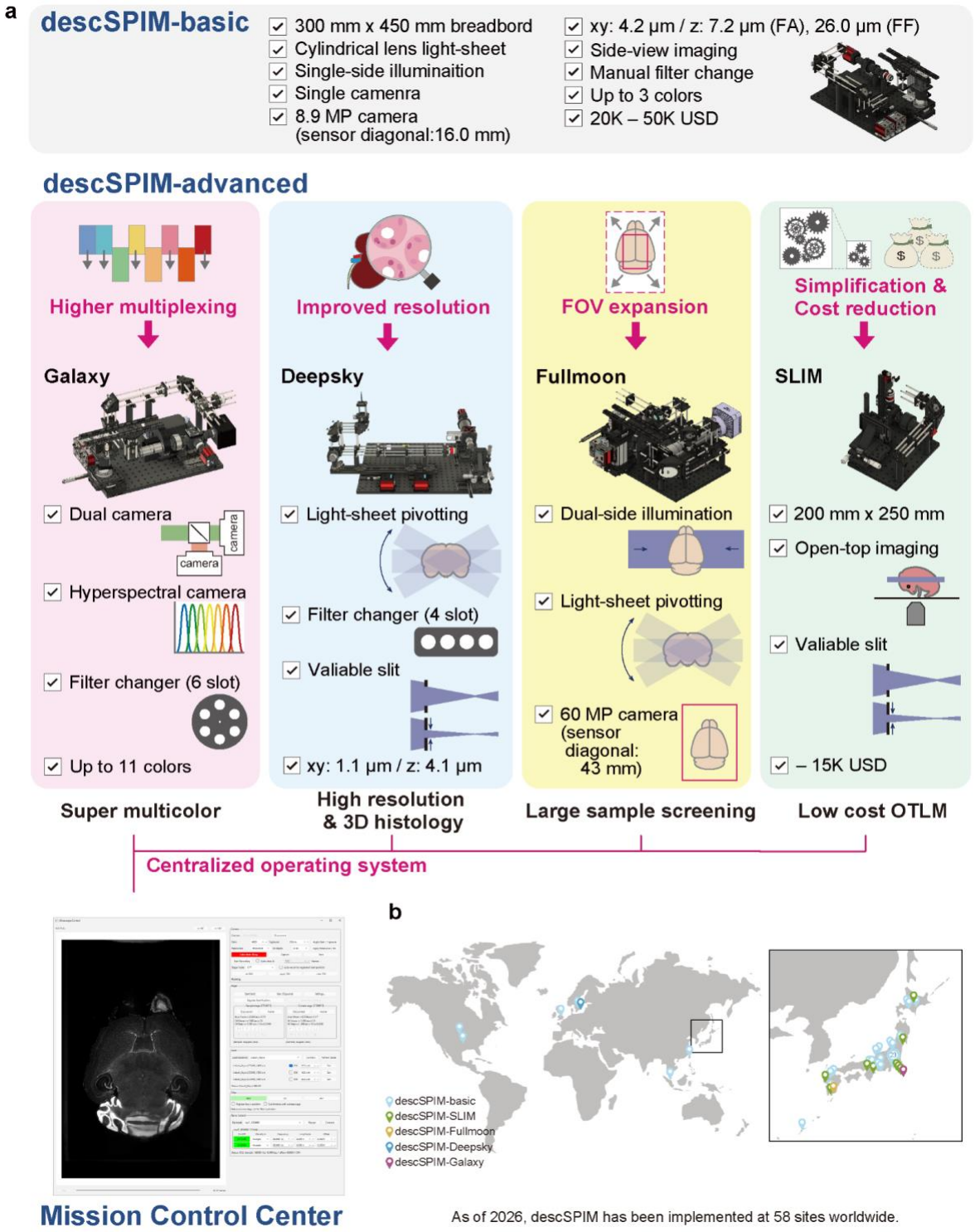


Fig. 6 | Democratizing cleared-tissue imaging from low-end to high-end through the expanded descSPIM ecosystem

a, Conceptual overview of the descSPIM-Advanced ecosystem. The descSPIM-basic is a DIY-based light-sheet microscopy system for cleared-tissue imaging that was designed to provide

an affordable, easy-to-build and deployable entry point for individual laboratories. Building on the expandable modular architecture of the original design, we expanded the application space of descSPIM in four directions: higher multiplexing, improved resolution, larger sample size, and simplified, lower-cost implementation. Middle panels show the descSPIM-Advanced variants corresponding to these four dimensions—Galaxy, Deepsky, Fullmoon, and SLIM—together with the newly introduced features for each variant. These systems can all be commanded through Mission Control Center (MCC), a shared control software platform. **b,** Global implementation map of descSPIM variants, including descSPIM-basic and descSPIM-Advanced systems. Sites are color-coded by installed variants: sky blue, descSPIM-basic; green, descSPIM-SLIM; yellow, descSPIM-Fullmoon; blue, descSPIM-Deepsky; magenta, descSPIM-Galaxy. The map shows 58 descSPIM implementation sites worldwide, highlighting the dissemination of the descSPIM ecosystem across routine and advanced cleared-tissue imaging applications.

Supplementary Files

This is a list of supplementary files associated with this preprint. Click to download.

- SupplementarymaterialsofdescSPIMAdvancedpaper.pdf